

DUST-OBSCURED GALAXIES IN THE LOCAL UNIVERSE

HO SEONG HWANG AND MARGARET J. GELLER

Smithsonian Astrophysical Observatory, 60 Garden St., Cambridge, MA 02138

Last updated: August 22, 2018

ABSTRACT

We use *Wide-field Infrared Survey Explorer* (*WISE*), *AKARI*, and *Galaxy Evolution Explorer* (*GALEX*) data to select local analogs of high-redshift ($z \sim 2$) dust obscured galaxies (DOGs). We identify 47 local DOGs with $S_{12\mu\text{m}}/S_{0.22\mu\text{m}} \geq 892$ and $S_{12\mu\text{m}} > 20$ mJy at $0.05 < z < 0.08$ in the Sloan Digital Sky Survey data release 7. The infrared luminosities of these DOGs are in the range $3.4 \times 10^{10} (L_{\odot}) \lesssim L_{\text{IR}} \lesssim 7.0 \times 10^{11} (L_{\odot})$ with a median L_{IR} of $2.1 \times 10^{11} (L_{\odot})$. We compare the physical properties of local DOGs with a control sample of galaxies that have lower $S_{12\mu\text{m}}/S_{0.22\mu\text{m}}$ but have similar redshift, IR luminosity, and stellar mass distributions. Both *WISE* 12 μm and *GALEX* near-ultraviolet (NUV) flux densities of DOGs differ from the control sample of galaxies, but the difference is much larger in the NUV. Among the 47 DOGs, $36 \pm 7\%$ have small axis ratios in the optical (i.e., $b/a < 0.6$), larger than the fraction among the control sample ($17 \pm 3\%$). There is no obvious sign of interaction for many local DOGs. No local DOGs have companions with comparable optical magnitudes closer than ~ 50 kpc. The large- and small-scale environments of DOGs are similar to the control sample. Many physical properties of local DOGs are similar to those of high- z DOGs, even though the IR luminosities of local objects are an order of magnitude lower than for the high- z objects: the presence of two classes (active galactic nuclei- and star formation-dominated) of DOGs, abnormal faintness in the UV rather than extreme brightness in the mid-infrared, and diverse optical morphology. These results suggest a common underlying physical origin of local and high- z DOGs. Both seem to represent the high-end tail of the dust obscuration distribution resulting from various physical mechanisms rather than a unique phase of galaxy evolution.

Subject headings: galaxies: active – galaxies: evolution – galaxies: formation – galaxies: starburst – infrared: galaxies – surveys

1. INTRODUCTION

Understanding how the star formation activity of galaxies evolves with cosmic time is one of the key issues in the study of galaxy formation and evolution. Redshift $z \sim 2$ is an interesting epoch because most of the stellar mass in galaxies today formed around this epoch (Dickinson et al. 2003) and because the cosmic star formation rate density also peaked (e.g., Behroozi et al. 2012). Interestingly, most star formation at this epoch took place in dusty galaxies, and the infrared luminosity from dust is higher than the observed ultraviolet (UV) luminosity even in UV selected galaxies (Reddy et al. 2008, 2012). It is thus important to study $z \sim 2$ dusty galaxies to understand what drives the intense star formation at this epoch.

One way to identify high- z dusty objects is to select optically faint, mid-infrared bright galaxies (e.g., Yan et al. 2004; Dey et al. 2008; Fiore et al. 2008; Lonsdale et al. 2009; Sajina et al. 2012). A color selection of $(R - [24]) \geq 14$ (mag in Vega, or $S_{24\mu\text{m}}/S_{0.65\mu\text{m}(R)} \geq 982$) produces a sample of $z \sim 2$ star-forming galaxies with large dust obscuration: dust-obscured galaxies (DOGs, Dey et al. 2008; Fiore et al. 2008; Penner et al. 2012; Hwang et al. 2012b). As the name suggests, optical spectra reveal that DOGs suffer from severe extinction (Brand et al. 2007; Melbourne et al. 2011). The amount of extinction inferred from the Balmer decrement (i.e., $H\alpha/H\beta$) is $A(H\alpha) \sim 2.4 - 4.6$, much larger than for other galaxies at similar redshift, but comparable with submillime-

ter galaxies (Takata et al. 2006) or with extreme local ultraluminous infrared galaxies (ULIRGs; Veilleux et al. 2009).

The rest-frame near-infrared (NIR) spectral energy distributions (SEDs) of these DOGs suggest that there are two types of DOGs: “bump” and “power-law” DOGs (Dey et al. 2008). Bump DOGs are generally fainter than power-law DOGs at 24 μm (e.g., $S_{24\mu\text{m}} < 0.8$ mJy). Their SEDs show a rest-frame 1.6 μm bump caused by a minimum in the opacity of the H^- ion present in the atmospheres of cool stars. Their mid-infrared (MIR) spectra show strong polycyclic aromatic hydrocarbon (PAH) emission (Pope et al. 2008; Desai et al. 2009), a typical feature of ongoing star formation. In contrast, the NIR/MIR SEDs of power-law DOGs show a rising continuum (i.e., power-law shape), and usually do not contain PAH emission (Houck et al. 2005). The power-law continuum is usually attributed to a hot dust component, indicating the presence of active galactic nuclei (AGN). The rest-frame UV/optical images reveal that bump DOGs are generally larger than power-law DOGs, and have more diffuse and irregular morphologies (Melbourne et al. 2009; Donley et al. 2010; Busmann et al. 2009a, 2011). Clustering analysis of these DOGs suggests that more luminous ones at 24 μm tend to reside in richer environments (i.e., strongly clustered) than less luminous ones (Brodwin et al. 2008).

Recent observational efforts have extended the study of DOGs to the far-infrared (FIR) and submillimeter regimes, providing a better view of their infrared properties (Pope et al. 2008; Tyler et al. 2009; Busmann et al.

2009b; Melbourne et al. 2012; Penner et al. 2012). For example, Penner et al. (2012) found that the specific star formation rates (sSFR, i.e., SFR per unit stellar mass) of DOGs are similar to the majority of typical star-forming galaxies at similar redshift (but see also Melbourne et al. 2012). They also suggest that the extreme ratios between rest-frame MIR and UV flux densities mainly result from abnormal faintness in the UV rather than abnormal brightness in the MIR.

Physical models for the formation and evolution of DOGs account for several observational features including IR luminosity, dust temperature, and stellar mass (e.g., Narayanan et al. 2010). Using numerical simulations, Narayanan et al. conclude that DOGs are a diverse population ranging from secularly evolving star-forming disk galaxies to extreme gas-rich galaxy mergers. They further suggest that some DOGs seem to be a transition phase in the evolutionary sequence of galaxy mergers; the sequence progresses from submillimeter galaxies to DOGs to quasars to elliptical galaxies. However, because of their extreme distances, it is difficult to compare detailed observational features with model predictions.

In this study, we search for local analogs of high- z DOGs. We study their physical properties in detail by taking advantage of their proximity and of the wealth of multiwavelength data. The local DOGs are useful testbeds for studying the evolutionary significance, and for providing an important hint of the nature of their high- z counterparts. We also construct a control galaxy sample with distributions of physical parameters (e.g., redshift, IR luminosity, stellar mass) similar to local DOGs, but not satisfying the DOG criterion.

Section 2 describes the observational data and the method we use to identify both local analogs of DOGs and the control sample of galaxies. We compute the IR luminosities and the AGN contribution of local DOGs in Section 3. We compare several physical parameters of local DOGs with the control sample and with high- z DOGs in Sections 4 and 5, respectively. We discuss the results and conclude in Sections 6 and 7, respectively. Throughout, we adopt flat Λ CDM cosmological parameters: $H_0 = 70 \text{ km s}^{-1} \text{ Mpc}^{-1}$, $\Omega_\Lambda = 0.7$ and $\Omega_m = 0.3$. All magnitudes are on the AB magnitude system. SDSS *ugriz* data are Petrosian magnitudes unless otherwise noted. When we convert SDSS magnitudes into AB magnitudes for the SED fit, we adopt the offset used in Kcorrect (v4.2) software of Blanton & Roweis (2007): $\Delta m = m_{\text{AB}} - m_{\text{SDSS}} = -0.036, 0.012, 0.010, 0.028, 0.040$ for *ugriz* bands.

2. SAMPLE SELECTION

2.1. Multiwavelength Data

We use a spectroscopic sample of galaxies and quasars in the Sloan Digital Sky Survey (SDSS; York et al. 2000) data release 9 (DR9, Ahn et al. 2012). The spectroscopic completeness of the SDSS data is poor for bright galaxies with $m_r < 14.5$ and for galaxies in high-density regions. Thus, we supplement the galaxy data by compiling redshifts for the photometric sample of galaxies with $m_r < 17.77$ from the literature (see Hwang et al. 2010a for details).

For this SDSS sample, we compile the available multi-wavelength photometric data from far-UV (FUV) to FIR.

We first add the *Galaxy Evolution Explorer* (GALEX; Martin et al. 2005) UV data from the GALEX general release 6 (GR6¹) that provides the cross-matched table (xSDSSDR7) against SDSS DR7². The matching tolerance is $5''$ (\sim FWHM of the GALEX PSF). To avoid contamination by nearby sources within the matching tolerance, we select only unique matches; for a given SDSS object, we choose the GALEX object closest to the SDSS object and vice versa.

The GALEX GR6 contains several imaging survey databases including the Nearby Galaxy Survey (NGS), Deep (DIS), Medium (MIS), and All Sky Surveys (AIS). We use all the sources covered by these surveys. The typical exposure time for the shallowest survey (i.e., AIS) is $\sim 100 \text{ s}$ corresponding to 5σ limiting magnitudes of $m_{\text{FUV}} \sim 20$ and $m_{\text{NUV}} \sim 20.8$. We correct for Galactic extinction following Wyder et al. (2007). Apertures for GALEX photometry are not matched to the bands in other wavelengths, but they are large enough to contain most of galaxy light. Thus aperture correction is unnecessary (Ree et al. 2007).

We adopt the NIR data from the extended source catalog (Jarrett et al. 2000) of the Two Micron All Sky Survey (2MASS; Skrutskie et al. 2006). The matching tolerance is $1.5''$ (Obrić et al. 2006). We use *JHK_s* 20 mag arcsec⁻² isophotal fiducial elliptical aperture magnitudes (AB).

We include the MIR data from the all-sky survey catalog³ of the *Wide-field Infrared Survey Explorer* (WISE; Wright et al. 2010), containing uniform photometric data for over 563 million objects at 4 MIR bands (3.4, 4.6, 12 and 22 μm). We identify WISE counterparts of SDSS objects with a matching tolerance of $3''$ ($\sim 0.5 \times$ FWHM of the WISE PSF at 3.4 μm). Because of the high number density of WISE sources, we use $0.5 \times$ FWHM as a matching tolerance rather than $1 \times$ FWHM; the expected false detection rate with $3''$ tolerance is only 0.05% (Donoso et al. 2012). We use the point source profile-fitting magnitudes. WISE 5σ photometric sensitivity is estimated to be better than 0.08, 0.11, 1 and 6 mJy at 3.4, 4.6, 12 and 22 μm in unconfused regions on the ecliptic plane (Wright et al. 2010).

We also add 9 and 18 μm flux density measurements from the all-sky survey Point Source Catalog (PSC ver. 1.0, Ishihara et al. 2010) of the AKARI telescope (Murakami et al. 2007). The 5σ detection limits at 9 and 18 μm are 50 and 90 mJy, respectively.

We obtain the FIR data by cross-correlating the SDSS sample with the *Infrared Astronomical Satellite* (IRAS; Neugebauer et al. 1984) Faint Sources Catalog ver. 2 (Moshir et al. 1992; with 12, 25, 60 and 100 μm bands) and the AKARI/Far-Infrared Surveyor (FIS; Kawada et al. 2007) all-sky survey Bright Source Catalog (BSC)⁴ ver. 1.0 (with 65, 90, 140 and 160 μm bands).

¹ <http://galex.stsci.edu/GR6>

² Because we use the GALEX GR6 catalog based on SDSS DR7, the SDSS sample in this study is actually equivalent to DR7 rather than DR9, even though all the photometric parameters are adopted from DR9 (see Ahn et al. 2012 for details about the difference between DR9 and DR7).

³ <http://wise2.ipac.caltech.edu/docs/release/allsky/expsup/>

⁴ <http://www.ir.isas.jaxa.jp/AKARI/Observation/PSC/Public/RN/AKARI-FIS-BSC-V1.LRN.pdf>

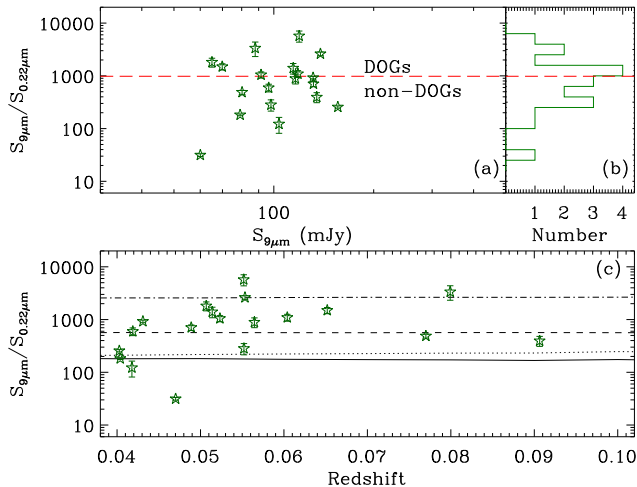


Figure 1. Flux density ratio between *AKARI* 9 μm and *GALEX* NUV observations of SDSS galaxies as a function of 9 μm flux density (a), and its histogram (b). The flux density ratio as a function of redshift (c). The long dashed line in (a) indicates the selection criterion for local DOGs ($S_{9\mu\text{m}}/S_{0.22\mu\text{m}} = 982$). In the bottom panel, we overplot the expected ratios from several SED templates for local star-forming, or AGN-host galaxies (Polletta et al. 2007, M82: solid, Arp220: dotted, Mrk 231: dashed, IRAS 19254-7245 South: dash dot).

2.2. *AKARI* 9 μm Selected Local DOGs

To identify local analogs of DOGs, we first use *GALEX* NUV ($\sim 0.22 \mu\text{m}$) and *AKARI* 9 μm data for the SDSS galaxies at $z < 0.1$. These data are roughly equivalent to the *R*-band ($0.65 \mu\text{m}$) and *Spitzer* 24 μm data originally used for selecting $z \sim 2$ DOGs (Dey et al. 2008).

We plot the flux density ratio between the *AKARI* 9 μm and *GALEX* NUV as a function of 9 μm flux density in the top panel of Figure 1. We restrict our analysis to galaxies with $0.04 < z < 0.1$. The lower limit is set by the small, fixed-size ($3''$) aperture for the SDSS spectra covering only a small ($< 20\%$) portion of the entire galaxy light at $z < 0.04$ (Kewley et al. 2005). The upper limit selects bright galaxies so that visual inspection of galaxy morphology in the SDSS image is reliable.

We show the Dey et al. criterion (i.e., rest-frame MIR and UV flux density ratio ≥ 982) as a long dashed line in the top panels of Figure 1. Because of the difference in bandpasses between *AKARI* 9 μm and *Spitzer* 24 μm observation at $z \sim 2$ (i.e., 8 μm), the *AKARI* 9 μm flux density for local DOG selection could be smaller by $\sim 10\%$ (i.e., $S_{9\mu\text{m}}/S_{0.22\mu\text{m}} \gtrsim 0.9 \times 982$) if we assume the M82 SED at $z \sim 0.07$. However, we retain the $S_{9\mu\text{m}}/S_{0.22\mu\text{m}} \geq 982$ as our selection criterion for local DOGs. Among the 19 galaxies in the figure, eight satisfy the DOG criterion.

We also show the redshift dependence of the flux density ratio between *AKARI* 9 μm and *GALEX* NUV in the bottom panel of Figure 1. We overplot the flux density ratios expected from several SED templates of local star-forming, or AGN-host galaxies (Polletta et al. 2007, M82: solid, Arp220: dotted, Mrk 231: dashed, IRAS 19254-7245 South: dash dot). Interestingly, none of these templates except IRAS 19254-7245 South⁵ sat-

⁵ IRAS 19254-7245 South satisfies the DOG criterion, but the relevant UV SED of this galaxy is not well constrained (see Berta et al. 2003).

isfy the DOG criterion (see also Figure 1 in Dey et al. 2008).

2.3. *WISE* 12 μm Selected Local DOGs

2.3.1. Selection Criteria

To identify additional local DOGs missed by the shallow *AKARI* MIR all-sky survey, we use *WISE* 12 μm data instead of *AKARI* 9 μm data. We show the flux density ratio between *WISE* 12 μm and *GALEX* NUV data as a function of the 12 μm flux density in the top panel of Figure 2. To determine an optimal parameter space for selecting local DOGs, we first plot the *AKARI* 9 μm detected DOGs as green star symbols. All eight objects are detected at 12 μm . The minimum flux density ratio for these objects is $S_{12\mu\text{m}}/S_{0.22\mu\text{m}} \sim 892$, and they are in the redshift range $0.05 < z < 0.08$ (bottom panel⁶).

We then select *WISE* 12 μm detected local DOGs that share the same parameter space as the *AKARI* 9 μm selected DOGs (i.e., $S_{12\mu\text{m}}/S_{0.22\mu\text{m}} \geq 892$ and $0.05 < z < 0.08$). Among these, we consider only 47 bright 12 μm sources with $S_{12\mu\text{m}} > 20$ mJy for further analysis (red filled circles). Including the galaxies fainter than $S_{12\mu\text{m}} = 20$ mJy does not change our conclusions, but for comparison with high- z DOGs we specialize to the more luminous local analogs.

2.3.2. The Control Sample of Galaxies

To compare the physical properties of these extremely dusty galaxies with other local galaxies, we construct a control sample. We first select a preliminary control sample of galaxies that are in the same range of redshift ($0.05 < z < 0.08$) and 12 μm flux density ($S_{12\mu\text{m}} \geq 21.79$ mJy⁷) as the *WISE* 12 μm detected local DOGs. These control objects do not satisfy the DOG criterion (i.e., $S_{12\mu\text{m}}/S_{0.22\mu\text{m}} < 892$, gray diamonds in Figure 2).

To have an unbiased control sample, the redshift, IR luminosity, and stellar mass distributions of the control sample should match those of local DOGs. We first examine the redshift distribution using the Kolmogorov-Smirnov (K-S) test to determine whether the DOGs and the control sample are drawn from the same distribution. The K-S test cannot reject the hypothesis that the redshift distributions of the two samples are extracted from the same parent population. We then compare the IR luminosities (L_{IR}) and stellar masses (M_{star}) of the two samples in Figure 3 (DOGs: red circles, control: gray diamonds). We compute the IR luminosities of DOGs and the control sample from the SED fit to the IR photometric data. We explain the details of this fitting in the next section. Stellar mass estimates are adopted from the MPA/JHU DR7 value-added galaxy catalog⁸ (VAGC). These estimates are based on the fit of SDSS five-band photometry to the models of Bruzual & Charlot (2003)

⁶ There are three *AKARI* 9 μm and 85 *WISE* 12 μm selected galaxies at $z > 0.1$ that satisfy our selection criteria. Because of their broad redshift range ($0.1 \lesssim z \lesssim 2.5$), the observational data probe different wavelengths. Therefore, we do not include them in the analysis.

⁷ We select the local DOGs with $S_{12\mu\text{m}} > 20$ mJy, but the minimum $S_{12\mu\text{m}}$ for the local DOGs is actually 21.79 mJy. Therefore, we use $S_{12\mu\text{m}} \geq 21.79$ mJy to construct a control sample of galaxies.

⁸ <http://www.mpa-garching.mpg.de/SDSS/DR7/Data/stellarmass.html>

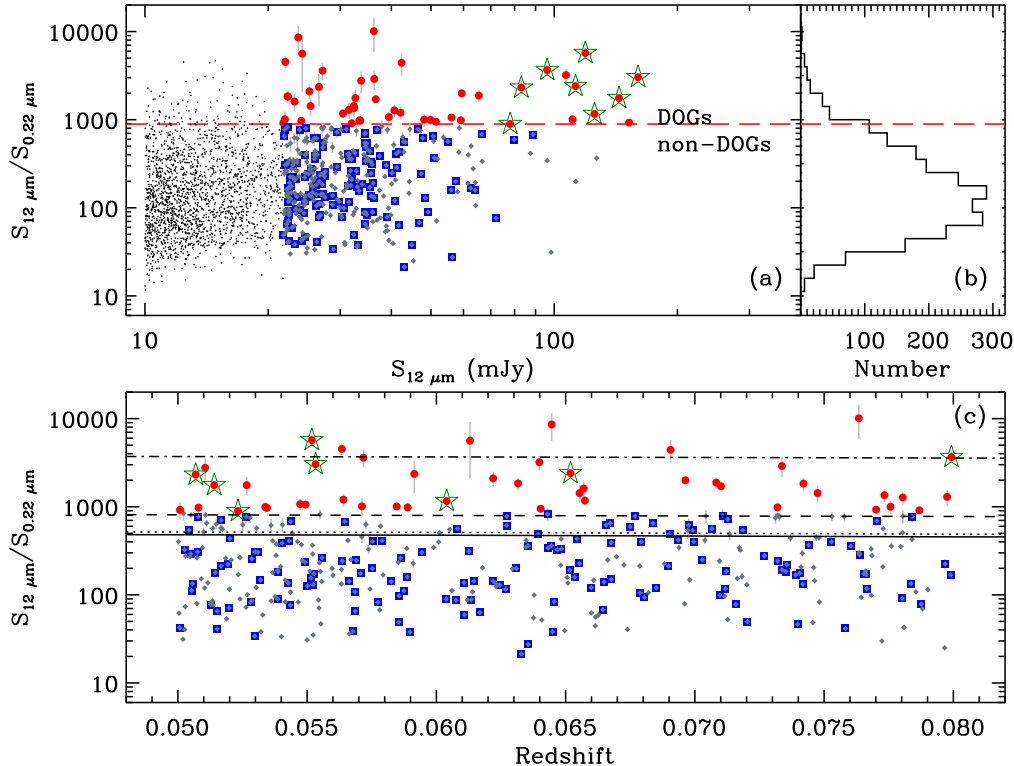


Figure 2. Flux density ratio between *WISE* 12 μm and *GALEX* NUV observations for SDSS galaxies (black dots) as a function of 12 μm flux density (a), and its histogram (b). Flux density ratio as a function of redshift (c). Green star symbols are *AKARI* 9 μm selected local DOGs. Red filled circles are *WISE* 12 μm selected local DOGs, and gray diamonds are the preliminary control sample of galaxies. Blue squares are the final control sample of galaxies determined in Figure 3. We plot error bars only for local DOGs. The long dashed line in (a) indicates the selection criterion for these local DOGs ($S_{12\mu\text{m}}/S_{0.22\mu\text{m}} = 892$). In the bottom panel, we overplot the expected ratios from several SED templates for local star-forming, or AGN-host galaxies (Polletta et al. 2007, M82: solid, Arp220: dotted, Mrk 231: dashed, IRAS 19254-7245 South: dash dot).

(see also Kauffmann et al. 2003a). We convert the stellar masses in the MPA/JHU DR7 VAGC that are based on the Kroupa IMF (Kroupa 2001) to those with a Salpeter IMF (Salpeter 1955) by dividing them by a factor of 0.7 (Elbaz et al. 2007).

For the IR luminosity distribution, the K-S test rejects the hypothesis that the distributions of the two samples are extracted from the same parent population with a confidence level of 99.9%. Therefore, we revise the construction of the control sample by randomly selecting galaxies among the preliminary control sample of galaxies (i.e., gray diamonds) to have the same IR luminosity distribution as the DOGs. We restrict this process to galaxies in the same range of IR luminosity and stellar mass as the DOGs (i.e., those within the dashed box). We set the number of control sample objects to be three times the number of DOGs (i.e., 141 galaxies in the control sample). The resulting distributions of redshift, IR luminosity, and stellar mass for the control sample are similar to those for the 47 DOGs, according to K-S tests. We show these 141 control sample of galaxies with blue squares in Figures 2 and 3.

3. ANALYSIS OF SPECTRAL ENERGY DISTRIBUTIONS OF LOCAL DOGS

3.1. Spectral Energy Distribution Modeling

We compute the IR luminosities of DOGs and the control sample using the SED templates and fitting routine

of Mullaney et al. (2011), DECOMP⁹. This routine requires observational data at $\lambda > 6 \mu\text{m}$ for the fit; we use measured flux densities of *WISE* 12 and 22 μm , *AKARI* 9, 18, 65, 90, 140 and 160 μm , *IRAS* 12, 25, 60 and 100 μm . We use only reliable flux density measurements; flux quality flags are either ‘high’ or ‘moderate’ for the *IRAS* data and ‘high’ for the *AKARI* data, and we require signal-to-noise ratios (S/Ns) ≥ 3 for *WISE* data. Because some bands partially overlap (e.g., *WISE* 12 μm and *IRAS* 12 μm , *IRAS* 60 μm and *AKARI* 65 μm , and *IRAS* 100 μm and *AKARI* 90 μm), we use only one measurement (i.e., *WISE* 12 μm , *IRAS* 60 μm and 100 μm) for the fit to avoid over-weighting when both flux densities are measured.

For a given galaxy, this routine decomposes the observed SED into two components (i.e., a host-galaxy and an AGN). We can thus measure the contribution of (buried) AGN to the total infrared energy budget of a galaxy. The SED templates consist of one AGN SED and five groups of host-galaxy SEDs, referred to as ‘SB1’ through ‘SB5’. These templates are constructed from *Spitzer* infrared spectrograph (IRS) spectra and *IRAS* photometric data of AGN-host and starburst galaxies (Mullaney et al. 2011).

We apply this routine to the DOGs and the control sample, and choose the best-fit solution with the lowest χ^2 value for each galaxy. We compute the uncertainties in the IR luminosity and in the AGN contribution

⁹ <http://sites.google.com/site/decompir>

Table 1
Properties of *WISE* 12 μ m Selected DOGs

ID	SDSS ObjID (DR9)	R.A. ₂₀₀₀	Decl. ₂₀₀₀	z	M _{star} ^a ($\times 10^{10} M_{\odot}$)	L _{IR} ($\times 10^{10} L_{\odot}$)	f _{AGN} (%)	CLASS ^b
1	1237663783124992102	00:12:26.83	-00:48:19.45	0.0734	11.11 \pm 2.71	37.72 \pm 3.54	0 \pm 0	C
2	1237652900763861074	02:25:33.60	-08:25:17.80	0.0549	...	22.18 \pm 0.25	0 \pm 0	h
3	1237663789024739682	07:25:28.47	+43:43:32.39	0.0691	10.55 \pm 2.63	>6.86	<100	S
4	1237653587407536295	08:03:37.33	+39:26:33.13	0.0655	29.78 \pm 7.45	>5.43	<100	S
5	1237654382512111741	08:42:11.60	+48:18:36.31	0.0563	1.58 \pm 0.38	13.26 \pm 0.16	0 \pm 0	U
6	1237657118948393018	08:42:15.29	+40:25:33.29	0.0553	3.83 \pm 1.34	16.43 \pm 0.18	100 \pm 0	S
7	1237674462024106294	09:04:01.02	+01:27:29.12	0.0534	12.82 \pm 3.08	38.10 \pm 0.49	0 \pm 0	C
8	1237674460413690092	09:07:46.91	+00:34:30.55	0.0534	4.16 \pm 1.01	9.02 \pm 0.12	0 \pm 0	S
9	1237663530802937978	09:38:19.17	+64:37:21.26	0.0710	21.32 \pm 4.37	50.69 \pm 0.65	0 \pm 0	C
10	1237661064416591910	10:01:40.47	+09:54:31.54	0.0564	4.74 \pm 1.08	7.43 \pm 0.46	51 \pm 6	S
11	1237665099004248259	10:07:07.58	+31:01:57.00	0.0501	5.14 \pm 1.21	7.05 \pm 0.09	0 \pm 0	H
12	1237667254540042377	10:09:45.63	+26:11:50.54	0.0747	4.15 \pm 0.93	>5.13	<100	S
13	1237661383848951984	10:11:01.09	+38:15:19.74	0.0527	3.56 \pm 0.76	16.78 \pm 0.22	0 \pm 0	C
14	1237654605860110514	10:17:31.29	+04:36:19.04	0.0572	11.55 \pm 2.84	18.09 \pm 0.83	4 \pm 1	H
15	1237671262281662602	10:17:53.90	+15:56:03.73	0.0787	15.25 \pm 3.51	30.04 \pm 1.07	13 \pm 2	H
16	1237648722831868077	10:33:33.15	+01:06:35.15	0.0657	9.44 \pm 2.33	26.75 \pm 1.88	6 \pm 2	H
17	1237664337173610611	10:44:45.46	+34:15:10.58	0.0708	13.09 \pm 3.09	21.72 \pm 1.22	38 \pm 4	S
18	1237665128536408188	10:56:53.37	+33:19:45.68	0.0511	3.90 \pm 0.91	14.41 \pm 1.11	0 \pm 0	S
19	1237651067886502124	11:02:13.01	+64:59:24.86	0.0776	24.70 \pm 6.07	32.26 \pm 1.09	10 \pm 2	S
20	1237657856606404709	11:08:52.62	+51:02:25.71	0.0696	12.84 \pm 3.07	24.35 \pm 0.94	23 \pm 3	S
21	1237651754005889185	11:19:34.25	+02:31:29.19	0.0508	5.81 \pm 1.31	8.25 \pm 0.73	26 \pm 6	S
22	123767114147777656	11:29:56.35	-06:24:20.48	0.0523	...	42.92 \pm 5.90	4 \pm 2	h
23	1237657611801657347	11:35:49.09	+56:57:08.27	0.0514	15.25 \pm 3.42	33.09 \pm 0.96	24 \pm 2	S
24	1237657856610271340	12:04:53.90	+52:23:43.39	0.0632	6.15 \pm 1.46	16.66 \pm 0.21	0 \pm 0	C
25	1237664292075143390	12:12:43.86	+16:11:06.09	0.0571	5.26 \pm 1.14	8.42 \pm 0.68	11 \pm 2	C
26	1237667209992732748	12:21:34.35	+28:49:00.12	0.0613	10.93 \pm 2.59	26.02 \pm 4.07	0 \pm 0	C
27	1237667736660017246	12:56:25.47	+23:20:55.05	0.0742	9.75 \pm 2.43	36.32 \pm 2.12	0 \pm 0	C
28	1237665129084092587	12:56:42.72	+35:07:29.92	0.0547	3.91 \pm 0.90	21.34 \pm 0.24	0 \pm 0	L
29	1237648704581795973	12:56:45.02	+00:11:17.61	0.0622	...	10.06 \pm 1.85	10 \pm 10	s
30	1237668589190381691	13:00:05.35	+16:32:14.80	0.0799	41.95 \pm 10.45	>21.29	<100	S
31	1237667447809114245	13:15:17.85	+24:38:08.97	0.0645	1.56 \pm 0.34	>3.42	<100	U
32	1237665531171373168	13:39:26.08	+25:35:19.80	0.0763	4.12 \pm 0.97	8.92 \pm 0.13	100 \pm 0	S
33	1237665430241149030	13:41:02.95	+29:36:42.86	0.0773	12.81 \pm 2.97	34.56 \pm 0.50	0 \pm 0	C
34	1237665549424132213	13:56:03.30	+25:31:12.82	0.0591	3.56 \pm 1.18	12.00 \pm 0.17	0 \pm 0	C
35	1237665430243704865	14:07:00.39	+28:27:14.67	0.0770	22.23 \pm 4.99	47.98 \pm 1.63	67 \pm 4	C
36	1237661212583002226	14:48:19.38	+44:32:32.76	0.0798	31.88 \pm 7.47	>7.41	<100	S
37	1237662236409462990	14:54:27.46	+06:47:19.63	0.0657	8.97 \pm 2.06	10.24 \pm 0.42	9 \pm 2	H
38	1237665350246924437	14:58:26.55	+24:58:15.46	0.0640	15.40 \pm 3.62	13.86 \pm 0.98	38 \pm 7	S
39	1237648705135051235	15:26:37.67	+00:35:33.50	0.0507	10.07 \pm 2.47	23.97 \pm 0.61	8 \pm 1	S
40	1237662305125204020	15:50:01.60	+27:49:00.49	0.0780	6.79 \pm 1.42	22.68 \pm 1.00	25 \pm 3	S
41	1237662663216070833	15:51:53.04	+27:14:33.65	0.0589	9.54 \pm 2.20	28.12 \pm 0.96	1 \pm 1	H
42	1237662262718235201	16:09:48.22	+04:34:52.90	0.0640	3.54 \pm 0.76	16.22 \pm 0.45	100 \pm 4	S
43	1237662336261816691	16:51:21.88	+21:55:26.22	0.0552	3.62 \pm 0.80	23.61 \pm 1.36	41 \pm 3	S
44	1237661387621073252	16:53:37.16	+30:26:09.76	0.0732	...	44.16 \pm 0.47	0 \pm 0	U
45	1237668681527132368	17:03:30.38	+45:40:47.15	0.0604	...	33.82 \pm 1.20	34 \pm 2	s
46	1237656530531254308	17:38:01.52	+56:13:25.81	0.0652	13.78 \pm 3.27	32.93 \pm 1.11	40 \pm 2	S
47	1237663478726328339	22:53:32.98	-00:24:42.75	0.0585	9.92 \pm 2.41	68.74 \pm 0.72	0 \pm 0	C

¹ Stellar masses for the galaxies without SDSS spectra are not available.

² Galaxy classification based on optical line ratios: H (SF), C (Composite), S (Seyfert), L (LINER), and U (Undetermined). The lower case letter gives the classification adopted from NED.

by randomly selecting flux densities at each band within the associated error distribution (assumed to be Gaussian) and then refitting. Figure 4 shows example SEDs of DOGs with the best-fit AGN (dotted line) and host-galaxy (dashed line) templates. For the DOG in the top panel (a), the estimated AGN contribution to the total IR luminosity is 23%; the optical spectral classification also indicates that this DOG is a Seyfert galaxy. The DOG in the middle panel (b) does not contain any AGN component, consistent with its optical spectral classification (i.e., star-forming).

Among 47 DOGs and 141 control sample of galaxies, 6 DOGs and 14 control sample of galaxies are not detected in the FIR bands (i.e., neither at *IRAS* 60 μ m nor at *AKARI* 90 μ m). These FIR undetected galaxies have photometric data only up to the *WISE* 22 μ m

band. These non-detections do not result from lack of coverage by the *IRAS* or *AKARI* all-sky surveys; they occur because the FIR flux densities for these objects are below the detection limits of *IRAS* or *AKARI*. Non-detection in the FIR bands means that the IR SEDs are mainly dominated by a hot AGN dust component that is peaked in the MIR bands rather than in the FIR bands. For these galaxies, we fit the SEDs with only an AGN template to estimate their IR luminosities. The measured IR luminosities then indicate lower limits to the total IR luminosities. Similarly, we set the AGN contribution to the total IR luminosity in these FIR undetected galaxies to be 100%. The bottom panel (c) in Figure 4 shows an SED representative of this example.

We list the 47 local analogs of DOGs in Table 1 along with their SDSS identification, Right Ascension, Dec-

Table 2
UV and Optical Photometry for *WISE* 12 μm Selected DOGs^a

ID	FUV (mag)	NUV (mag)	<i>u</i> (mag)	<i>g</i> (mag)	<i>r</i> (mag)	<i>i</i> (mag)	<i>z</i> (mag)
1	...	21.16 ± 0.27	18.61 ± 0.06	17.22 ± 0.01	16.48 ± 0.01	15.93 ± 0.01	15.73 ± 0.01
2	21.60 ± 0.20	19.59 ± 0.06	17.00 ± 0.04	15.56 ± 0.02	14.80 ± 0.01	14.37 ± 0.02	14.14 ± 0.01
3	21.69 ± 0.47	21.45 ± 0.32	18.70 ± 0.08	17.35 ± 0.03	16.52 ± 0.03	16.05 ± 0.02	15.75 ± 0.02
4	...	20.51 ± 0.26	17.39 ± 0.05	15.81 ± 0.02	15.02 ± 0.02	14.60 ± 0.01	14.34 ± 0.02
5	...	22.18 ± 0.17	19.07 ± 0.08	17.58 ± 0.01	16.89 ± 0.01	16.56 ± 0.01	16.35 ± 0.03
6	...	19.59 ± 0.04	18.11 ± 0.03	16.67 ± 0.01	16.14 ± 0.02	15.85 ± 0.05	15.64 ± 0.08
7	20.97 ± 0.34	19.65 ± 0.14	18.08 ± 0.06	16.60 ± 0.02	15.90 ± 0.01	15.43 ± 0.01	15.15 ± 0.02
8	20.05 ± 0.05	20.41 ± 0.05	18.69 ± 0.07	17.14 ± 0.01	16.48 ± 0.01	16.11 ± 0.01	15.86 ± 0.02
9	...	20.57 ± 0.09	18.07 ± 0.07	16.33 ± 0.01	15.52 ± 0.01	15.08 ± 0.01	14.76 ± 0.01
10	21.27 ± 0.45	20.04 ± 0.18	18.03 ± 0.04	16.51 ± 0.02	15.79 ± 0.02	15.39 ± 0.03	15.18 ± 0.02
11	...	20.47 ± 0.24	18.30 ± 0.07	16.97 ± 0.01	16.17 ± 0.01	15.77 ± 0.01	15.52 ± 0.02
12	21.54 ± 0.47	20.78 ± 0.23	19.33 ± 0.08	17.95 ± 0.01	17.18 ± 0.01	16.74 ± 0.01	16.44 ± 0.03
13	21.64 ± 0.42	20.73 ± 0.25	18.49 ± 0.06	17.16 ± 0.01	16.53 ± 0.01	16.21 ± 0.01	15.99 ± 0.02
14	...	21.71 ± 0.24	20.43 ± 0.37	17.49 ± 0.01	16.55 ± 0.01	16.01 ± 0.01	15.66 ± 0.02
15	21.04 ± 0.30	20.03 ± 0.11	18.24 ± 0.05	16.87 ± 0.01	16.15 ± 0.01	15.68 ± 0.01	15.54 ± 0.02
16	20.77 ± 0.21	20.37 ± 0.13	19.32 ± 0.28	17.59 ± 0.39	16.76 ± 0.36	16.25 ± 0.32	15.97 ± 0.29
17	21.48 ± 0.47	20.04 ± 0.15	18.09 ± 0.04	16.65 ± 0.01	15.90 ± 0.01	15.47 ± 0.01	15.22 ± 0.01
18	21.54 ± 0.47	21.18 ± 0.30	18.73 ± 0.07	17.07 ± 0.01	16.30 ± 0.02	15.90 ± 0.02	15.66 ± 0.02
19	20.20 ± 0.28	19.69 ± 0.18	18.55 ± 0.08	17.02 ± 0.03	16.19 ± 0.02	15.48 ± 0.02	15.37 ± 0.02
20	...	20.21 ± 0.11	18.25 ± 0.04	16.73 ± 0.02	15.98 ± 0.02	15.55 ± 0.02	15.30 ± 0.02
21	21.05 ± 0.15	20.06 ± 0.14	17.87 ± 0.06	16.46 ± 0.01	15.76 ± 0.01	15.39 ± 0.01	15.18 ± 0.02
22	20.43 ± 0.29	19.05 ± 0.07	17.16 ± 0.03	15.79 ± 0.01	15.04 ± 0.01	14.60 ± 0.01	14.30 ± 0.01
23	20.64 ± 0.23	19.12 ± 0.07	17.01 ± 0.03	15.41 ± 0.00	14.69 ± 0.00	14.32 ± 0.00	14.13 ± 0.01
24	...	21.19 ± 0.17	18.77 ± 0.05	17.10 ± 0.01	16.41 ± 0.01	16.03 ± 0.01	15.81 ± 0.02
25	...	20.56 ± 0.25	18.72 ± 0.09	16.81 ± 0.01	16.07 ± 0.01	15.69 ± 0.01	15.46 ± 0.01
26	...	22.31 ± 0.68	19.60 ± 0.10	17.89 ± 0.01	16.95 ± 0.01	16.43 ± 0.01	16.18 ± 0.03
27	21.97 ± 0.39	21.18 ± 0.18	18.98 ± 0.09	17.36 ± 0.01	16.53 ± 0.01	16.06 ± 0.01	15.77 ± 0.02
28	21.28 ± 0.38	19.98 ± 0.17	18.27 ± 0.07	16.94 ± 0.01	16.33 ± 0.01	15.99 ± 0.01	15.77 ± 0.03
29	22.63 ± 0.49	21.20 ± 0.21	19.14 ± 0.07	17.80 ± 0.01	17.08 ± 0.01	16.61 ± 0.01	16.40 ± 0.03
30	...	20.35 ± 0.15	18.08 ± 0.12	16.23 ± 0.01	15.31 ± 0.01	14.84 ± 0.01	14.59 ± 0.02
31	...	22.80 ± 0.37	19.82 ± 0.13	18.34 ± 0.02	17.55 ± 0.01	17.19 ± 0.01	16.97 ± 0.04
32	21.55 ± 0.46	22.51 ± 0.45	19.91 ± 0.11	18.35 ± 0.01	17.60 ± 0.01	17.06 ± 0.01	16.86 ± 0.03
33	21.11 ± 0.30	20.45 ± 0.18	18.42 ± 0.06	17.28 ± 0.01	16.56 ± 0.01	16.10 ± 0.01	15.94 ± 0.02
34	...	21.27 ± 0.43	19.07 ± 0.17	17.12 ± 0.01	16.40 ± 0.01	15.99 ± 0.01	15.82 ± 0.07
35	20.00 ± 0.05	18.36 ± 0.04	16.64 ± 0.02	15.38 ± 0.02	14.83 ± 0.02	14.39 ± 0.02	14.27 ± 0.01
36	20.52 ± 0.28	20.43 ± 0.22	17.66 ± 0.05	16.24 ± 0.01	15.29 ± 0.01	14.90 ± 0.01	14.67 ± 0.01
37	...	21.00 ± 0.25	20.43 ± 0.68	17.56 ± 0.02	16.73 ± 0.01	16.31 ± 0.01	15.98 ± 0.03
38	21.06 ± 0.45	19.57 ± 0.08	17.81 ± 0.05	16.29 ± 0.01	15.55 ± 0.01	15.13 ± 0.01	14.90 ± 0.01
39	...	20.01 ± 0.20	17.62 ± 0.04	16.06 ± 0.01	15.35 ± 0.01	14.96 ± 0.01	14.73 ± 0.01
40	21.19 ± 0.39	20.14 ± 0.18	18.61 ± 0.05	17.20 ± 0.02	16.49 ± 0.02	16.08 ± 0.02	15.89 ± 0.02
41	20.45 ± 0.31	20.07 ± 0.13	18.55 ± 0.09	16.99 ± 0.01	16.26 ± 0.01	15.77 ± 0.01	15.48 ± 0.03
42	20.90 ± 0.36	20.09 ± 0.20	18.59 ± 0.06	17.21 ± 0.03	16.56 ± 0.03	16.17 ± 0.02	15.93 ± 0.03
43	...	20.60 ± 0.17	18.74 ± 0.04	17.24 ± 0.01	16.56 ± 0.00	16.10 ± 0.00	15.89 ± 0.01
44	20.62 ± 0.29	19.45 ± 0.08	17.56 ± 0.02	16.10 ± 0.01	15.36 ± 0.00	14.89 ± 0.00	14.67 ± 0.01
45	19.50 ± 0.16	18.82 ± 0.08	17.60 ± 0.02	16.20 ± 0.01	15.52 ± 0.01	15.03 ± 0.01	14.88 ± 0.01
46	20.80 ± 0.23	19.72 ± 0.08	17.70 ± 0.05	16.24 ± 0.02	15.56 ± 0.02	15.16 ± 0.01	14.94 ± 0.02
47	20.17 ± 0.24	18.80 ± 0.08	17.41 ± 0.03	16.27 ± 0.02	15.66 ± 0.05	15.22 ± 0.07	15.04 ± 0.08

¹ All magnitudes are Galactic extinction-corrected AB magnitudes. SDSS *ugriz* data are Petrosian magnitudes.

lination, spectroscopic redshift, stellar mass, IR luminosity, AGN contribution to the total IR luminosity, and emission line classification. We also list the relevant UV/optical photometric data in Table 2, NIR/MIR photometric data in Table 3, and MIR/FIR photometric data in Table 4. With these photometric data, we plot the observed SEDs of the 47 DOGs in Figure 5; this plot includes many examples of the three SED types in Figure 4.

We also show SDSS color images of all the DOGs in Figure 6. The figure shows a variety of optical morphologies among DOGs from those with merging features (e.g., ID: 7, 13, 16, 19, 47) to highly-inclined disk galaxies (e.g., ID: 3, 11, 21, 34, 37). Interestingly, there are some galaxies with large bulge/spheroids (e.g., ID: 4, 30, 36). There are other early-type galaxies with IR activity in the local universe (e.g., Knapp et al. 1989; Lee et al. 2010; Smith et al. 2012; Hwang et al. 2012a; Ko et al.

2013). All of these early-type DOGs have Seyfert optical spectra; they are not detected in the FIR bands, suggesting AGN-dominated SEDs (see Figure 5).

In Figure 7, we show the AGN contribution to the total IR luminosities of DOGs (red circles) and the control sample (blue squares) as a function of total IR luminosity. We plot FIR detected (filled symbols) and undetected (open symbols) galaxies separately. We show open symbols with arrows to represent the upper/lower limits for AGN contribution and total IR luminosities. There is no correlation between the AGN contribution and the total IR luminosity for the DOGs or for the control sample; in contrast, ULIRGs do show a correlation (Veilleux et al. 2009; Lee et al. 2012).

3.2. Comparison of AGN Diagnostics

To compare the measured AGN contribution with other AGN selection methods, we plot the optical line

Table 3
NIR and MIR Photometry for *WISE* 12 μm Selected DOGs

ID	J^a (mag)	H (mag)	K_s (mag)	3.4 μm (mJy)	4.6 μm (mJy)	9 μm (mJy)	12 μm^b (mJy)	12 μm^c (mJy)
1	15.37 ± 0.06	15.09 ± 0.06	14.96 ± 0.07	2.68 ± 0.06	2.34 ± 0.06	...	36.34 ± 0.57	...
2	13.82 ± 0.03	13.50 ± 0.04	13.46 ± 0.05	9.20 ± 0.19	7.21 ± 0.14	...	56.12 ± 0.83	...
3	15.42 ± 0.07	14.69 ± 0.06	14.20 ± 0.05	14.73 ± 0.33	21.81 ± 0.38	...	42.38 ± 0.62	...
4	14.28 ± 0.04	14.05 ± 0.05	14.08 ± 0.06	4.87 ± 0.10	5.85 ± 0.11	...	32.38 ± 0.48	...
5	16.24 ± 0.10	15.97 ± 0.12	16.00 ± 0.14	0.75 ± 0.02	1.08 ± 0.03	...	22.04 ± 0.37	...
6	14.54 ± 0.04	14.10 ± 0.04	13.50 ± 0.03	31.07 ± 0.66	55.49 ± 0.97	138.18 ± 9.69	160.23 ± 2.21	162.80 ± 27.68
7	14.85 ± 0.07	14.44 ± 0.06	14.33 ± 0.09	4.95 ± 0.11	4.90 ± 0.09	...	49.83 ± 0.78	...
8	15.46 ± 0.08	15.07 ± 0.06	15.03 ± 0.09	2.77 ± 0.06	2.32 ± 0.06	...	24.10 ± 0.40	...
9	14.46 ± 0.04	14.13 ± 0.04	14.06 ± 0.05	5.60 ± 0.11	4.86 ± 0.09	...	36.64 ± 0.54	...
10	15.01 ± 0.12	14.46 ± 0.11	14.33 ± 0.12	5.73 ± 0.12	9.15 ± 0.19	...	42.14 ± 0.66	...
11	15.16 ± 0.06	14.78 ± 0.07	14.76 ± 0.07	3.12 ± 0.07	2.43 ± 0.05	...	21.79 ± 0.36	...
12	16.03 ± 0.10	15.97 ± 0.12	15.80 ± 0.12	3.56 ± 0.08	7.05 ± 0.13	...	25.39 ± 0.42	...
13	15.66 ± 0.05	15.34 ± 0.06	15.28 ± 0.06	1.91 ± 0.04	2.13 ± 0.05	...	32.68 ± 0.54	...
14	15.07 ± 0.06	14.64 ± 0.05	14.64 ± 0.07	3.46 ± 0.07	2.74 ± 0.06	...	27.16 ± 0.53	...
15	15.23 ± 0.05	14.97 ± 0.06	14.84 ± 0.06	3.31 ± 0.07	2.65 ± 0.06	...	32.03 ± 0.53	...
16	15.50 ± 0.07	15.23 ± 0.08	15.06 ± 0.09	2.95 ± 0.07	2.64 ± 0.06	...	30.47 ± 0.48	...
17	14.78 ± 0.04	14.45 ± 0.04	14.05 ± 0.04	17.49 ± 0.37	29.63 ± 0.55	...	65.45 ± 0.90	...
18	15.30 ± 0.05	15.12 ± 0.05	15.08 ± 0.06	2.11 ± 0.05	3.36 ± 0.07	...	33.75 ± 0.50	...
19	14.89 ± 0.04	14.62 ± 0.05	14.47 ± 0.05	6.75 ± 0.14	11.78 ± 0.22	...	48.12 ± 0.66	...
20	14.87 ± 0.04	14.53 ± 0.05	14.48 ± 0.05	5.11 ± 0.11	9.19 ± 0.18	...	59.42 ± 0.82	103.40 ± 27.92
21	14.95 ± 0.06	14.54 ± 0.05	14.60 ± 0.08	5.03 ± 0.13	7.69 ± 0.18	...	33.60 ± 0.77	...
22	13.82 ± 0.04	13.48 ± 0.04	13.38 ± 0.05	9.63 ± 0.27	7.62 ± 0.20	91.51 ± 10.73	78.04 ± 1.51	...
23	13.79 ± 0.03	13.34 ± 0.03	13.00 ± 0.03	34.00 ± 0.69	47.14 ± 0.82	114.39 ± 24.69	143.99 ± 1.99	133.20 ± 30.64
24	15.64 ± 0.06	15.28 ± 0.07	15.29 ± 0.07	1.87 ± 0.04	1.64 ± 0.04	...	22.30 ± 0.35	...
25	15.20 ± 0.05	14.87 ± 0.06	14.86 ± 0.06	3.06 ± 0.07	3.81 ± 0.08	...	21.98 ± 0.34	...
26	15.78 ± 0.07	15.31 ± 0.08	15.10 ± 0.06	2.28 ± 0.05	2.20 ± 0.05	...	24.23 ± 0.40	...
27	15.17 ± 0.05	14.94 ± 0.06	14.72 ± 0.06	2.84 ± 0.06	2.44 ± 0.05	...	22.36 ± 0.41	...
28	15.55 ± 0.07	15.24 ± 0.08	15.30 ± 0.08	2.04 ± 0.05	3.75 ± 0.08	...	39.44 ± 0.62	...
29	6.42 ± 0.12	9.32 ± 0.17	...	25.23 ± 0.40	...
30	14.29 ± 0.04	13.89 ± 0.05	13.43 ± 0.04	27.77 ± 0.56	44.28 ± 0.86	87.88 ± 23.89	96.10 ± 1.33	...
31	2.73 ± 0.06	11.91 ± 0.23	...	23.70 ± 0.39	...
32	1.65 ± 0.04	4.05 ± 0.08	...	36.27 ± 0.57	...
33	15.45 ± 0.06	15.05 ± 0.07	15.04 ± 0.06	2.87 ± 0.06	2.77 ± 0.06	...	32.44 ± 0.51	...
34	3.41 ± 0.07	2.76 ± 0.06	...	26.62 ± 0.39	...
35	14.05 ± 0.03	13.80 ± 0.04	13.44 ± 0.04	36.50 ± 0.77	51.26 ± 0.99	80.22 ± 6.16	152.45 ± 2.11	...
36	14.37 ± 0.04	13.95 ± 0.04	13.72 ± 0.04	11.14 ± 0.23	14.16 ± 0.26	...	31.53 ± 0.46	...
37	15.42 ± 0.09	14.93 ± 0.07	14.86 ± 0.10	3.10 ± 0.06	2.70 ± 0.05	...	23.20 ± 0.34	82.53 ± 24.76
38	14.77 ± 0.06	14.39 ± 0.06	14.47 ± 0.08	4.70 ± 0.10	7.02 ± 0.14	...	51.42 ± 0.76	...
39	14.36 ± 0.04	14.06 ± 0.05	14.11 ± 0.07	6.94 ± 0.15	14.03 ± 0.27	65.10 ± 2.42	83.09 ± 1.15	...
40	15.58 ± 0.08	15.31 ± 0.10	15.01 ± 0.07	7.42 ± 0.16	12.78 ± 0.24	...	40.69 ± 0.60	...
41	15.02 ± 0.05	14.73 ± 0.06	14.47 ± 0.06	4.11 ± 0.08	3.45 ± 0.06	...	33.41 ± 0.46	...
42	15.76 ± 0.08	15.41 ± 0.08	15.15 ± 0.08	8.28 ± 0.18	17.02 ± 0.30	...	106.84 ± 1.48	158.00 ± 28.44
43	15.38 ± 0.06	14.95 ± 0.06	14.20 ± 0.04	20.87 ± 0.42	40.68 ± 0.75	119.23 ± 21.73	119.11 ± 1.65	137.00 ± 21.92
44	14.08 ± 0.03	13.76 ± 0.03	13.71 ± 0.03	8.04 ± 0.18	6.25 ± 0.13	...	59.15 ± 0.82	81.69 ± 21.24
45	13.88 ± 0.03	13.53 ± 0.04	13.26 ± 0.04	26.69 ± 0.54	37.00 ± 0.72	118.18 ± 15.25	125.41 ± 1.73	152.60 ± 22.89
46	14.71 ± 0.05	14.33 ± 0.06	14.24 ± 0.06	9.77 ± 0.21	22.65 ± 0.42	69.90 ± 7.95	112.70 ± 1.45	114.70 ± 14.91
47	14.74 ± 0.04	14.31 ± 0.05	14.40 ± 0.06	6.96 ± 0.13	11.79 ± 0.24	...	110.85 ± 1.23	...

¹ 2MASS magnitudes are 20 mag arcsec⁻² isophotal fiducial elliptical aperture magnitudes (AB). These magnitudes represent approximately 85% of the total flux of a galaxy (see <http://www.ipac.caltech.edu/2mass/releases/allsky/doc/sec2.3d3.html>).

² *WISE* 12 μm .

³ *IRAS* 12 μm .

ratios of DOGs (circles) and the control sample (squares) in the left panel of Figure 8. Different colored symbols represent different AGN contributions measured from the SED decomposition (color coded as shown by the color bar to the top). As expected, most galaxies with a small AGN contribution (purple symbols) lie in the regions of star-forming and composite galaxies; those with a large AGN contribution (greenish and reddish symbols) lie mostly in the AGN region.

We use these line ratio diagrams to determine the optical spectral classification of the DOGs listed in Table 1 and in Figure 5. We adopt the criteria of Kewley et al. (2006) based on the Baldwin-Phillips-Terlevich (BPT) emission-line ratio diagrams (Baldwin et al. 1981; Veilleux & Osterbrock 1987). For

galaxies with $S/Ns \geq 3$ in the strong emission-lines $H\beta$, $[\text{OIII}] \lambda 5007$, $H\alpha$, $[\text{NII}] \lambda 6584$, and $[\text{SII}] \lambda \lambda 6717, 6731$, we base the classification on their positions in the line ratio diagrams with $[\text{OIII}]/H\beta$ plotted against $[\text{NII}]/H\alpha$, $[\text{SII}]/H\alpha$, and $[\text{OI}]/H\alpha$. These classes are star-forming galaxies, Seyferts, low-ionization nuclear emission-line regions (LINERs), composite galaxies, and ambiguous galaxies (see Kewley et al. 2006 for more details). Composite galaxies host a mixture of star formation and AGN, and lie between the extreme starburst line (Kewley et al. 2001) and the pure star formation line (Kauffmann et al. 2003b) in the $[\text{OIII}]/H\beta$ vs. $[\text{NII}]/H\alpha$ line ratio diagram (see the left panel in Figure 8). Ambiguous galaxies are those classified as one type in one or two diagrams, but as another type in the other diagrams.

Table 4
MIR and FIR Photometry for *WISE* 12 μm Selected DOGs

ID	18 μm (mJy)	22 μm (mJy)	25 μm (mJy)	60 μm (Jy)	65 μm (Jy)	90 μm (Jy)	100 μm (Jy)	140 μm (Jy)
1	...	206.25 \pm 3.61	...	1.05 \pm 0.07	...	1.20 \pm 0.04
2	...	111.58 \pm 2.77	...	1.75 \pm 0.12	...	1.90 \pm 0.07	3.42 \pm 0.24	4.26 \pm 1.27
3	...	82.94 \pm 2.14
4	...	116.52 \pm 2.68
5	...	132.92 \pm 2.69	177.30 \pm 28.37	1.10 \pm 0.05	...	0.83 \pm 0.02	1.17 \pm 0.15	...
6	272.17 \pm 15.20	342.92 \pm 7.26	278.50 \pm 50.13	0.36 \pm 0.04
7	...	161.28 \pm 2.97	236.90 \pm 40.27	3.06 \pm 0.15	3.31 \pm 0.41	3.53 \pm 0.11	4.42 \pm 0.40	4.00 \pm 0.77
8	...	49.43 \pm 1.50	...	0.76 \pm 0.05	...	0.80 \pm 0.07	1.04 \pm 0.16	...
9	...	110.76 \pm 2.86	167.80 \pm 26.85	1.72 \pm 0.10	...	1.98 \pm 0.10	3.40 \pm 0.31	...
10	...	119.12 \pm 2.52	202.10 \pm 40.42	0.21 \pm 0.04
11	...	42.74 \pm 1.42	...	0.61 \pm 0.04	1.11 \pm 0.14	...
12	...	54.35 \pm 1.95
13	...	203.42 \pm 4.50	288.00 \pm 40.32	1.48 \pm 0.09	...	1.07 \pm 0.11	1.55 \pm 0.14	...
14	...	74.13 \pm 2.39	...	0.83 \pm 0.07	...	0.96 \pm 0.03	1.50 \pm 0.13	...
15	...	81.51 \pm 2.85	...	0.81 \pm 0.06	...	0.94 \pm 0.03
16	...	101.39 \pm 2.52	1.28 \pm 0.06
17	...	138.16 \pm 2.80	...	0.54 \pm 0.04	...	0.75 \pm 0.23	0.65 \pm 0.13	...
18	...	143.74 \pm 3.05	193.40 \pm 30.94	0.81 \pm 0.05	...	0.51 \pm 0.09	0.80 \pm 0.13	...
19	...	184.33 \pm 3.73	216.80 \pm 19.51	0.54 \pm 0.04	0.95 \pm 0.18	...
20	...	200.81 \pm 4.07	203.50 \pm 28.49	0.49 \pm 0.05	0.83 \pm 0.15	...
21	...	83.94 \pm 4.56	...	0.42 \pm 0.06	...	0.68 \pm 0.14	0.83 \pm 0.22	...
22	...	181.80 \pm 7.70	290.80 \pm 52.34	2.60 \pm 0.18	2.90 \pm 0.20	3.67 \pm 0.04	4.19 \pm 0.38	4.45 \pm 1.05
23	343.40 \pm 21.14	438.11 \pm 10.09	500.80 \pm 35.06	1.67 \pm 0.10	...	1.73 \pm 0.08	2.15 \pm 0.17	...
24	...	121.11 \pm 2.34	142.60 \pm 21.39	0.82 \pm 0.06	...	0.64 \pm 0.08	0.86 \pm 0.18	...
25	...	75.37 \pm 2.08	...	0.38 \pm 0.06
26	...	101.11 \pm 2.51	1.93 \pm 0.11	...	2.85 \pm 0.37
27	...	82.87 \pm 2.14	143.10 \pm 35.77	1.60 \pm 0.11	...	1.62 \pm 0.06	2.55 \pm 0.25	...
28	...	197.69 \pm 3.82	303.60 \pm 48.58	2.66 \pm 0.16	...	2.00 \pm 0.04	2.52 \pm 0.28	...
29	...	50.53 \pm 1.77	...	0.27 \pm 0.06	0.59 \pm 0.14	...
30	175.05 \pm 50.81	181.30 \pm 4.68
31	...	49.70 \pm 1.60
32	94.93 \pm 8.66	167.80 \pm 3.55	204.30 \pm 57.20	0.22 \pm 0.04
33	...	126.94 \pm 2.57	205.30 \pm 45.17	1.48 \pm 0.12	...	1.45 \pm 0.08	1.94 \pm 0.27	...
34	...	48.30 \pm 1.51	...	0.71 \pm 0.06	...	0.82 \pm 0.05	1.22 \pm 0.15	...
35	305.41 \pm 30.17	398.46 \pm 7.71	399.40 \pm 39.94	0.73 \pm 0.06	0.94 \pm 0.15	...
36	...	73.11 \pm 1.68
37	...	34.64 \pm 1.12	...	0.52 \pm 0.05	...	0.75 \pm 0.04	1.18 \pm 0.14	...
38	112.20 \pm 12.27	221.61 \pm 3.47	161.70 \pm 21.02	0.36 \pm 0.04
39	219.55 \pm 24.55	348.01 \pm 5.13	359.20 \pm 39.51	0.92 \pm 0.06	1.33 \pm 0.21	...
40	...	123.93 \pm 2.28	127.10 \pm 20.34	0.49 \pm 0.04	0.69 \pm 0.17	...
41	...	90.45 \pm 1.92	132.20 \pm 25.12	1.31 \pm 0.07	...	1.52 \pm 0.10	2.52 \pm 0.23	...
42	247.55 \pm 35.80	281.31 \pm 4.40	317.80 \pm 31.78	0.20 \pm 0.04
43	...	324.78 \pm 5.68	410.20 \pm 32.82	1.01 \pm 0.07	0.92 \pm 0.21	...
44	...	127.29 \pm 2.46	144.50 \pm 18.78	1.48 \pm 0.10	...	1.85 \pm 0.08	3.47 \pm 0.21	...
45	235.96 \pm 23.60	361.07 \pm 5.99	415.90 \pm 29.11	1.16 \pm 0.07	...	0.88 \pm 0.05	1.46 \pm 0.18	...
46	241.33 \pm 13.94	312.17 \pm 4.60	383.90 \pm 15.36	0.92 \pm 0.05	...	0.82 \pm 0.04	1.22 \pm 0.17	...
47	310.73 \pm 37.67	618.28 \pm 10.25	716.30 \pm 57.30	5.14 \pm 0.36	3.77 \pm 0.32	5.04 \pm 0.18	5.03 \pm 0.55	5.97 \pm 0.94

For four galaxies with ‘ambiguous’ type (ID: 17, 21, 36 and 40), we replace the galaxy classification with the one based only on the [OIII]/H β vs. [NII]/H α line ratio diagram. We assign ‘undetermined’ type to those that do not satisfy the S/N criteria. For seven galaxies that we cannot classify because of a low S/N spectrum or the absence of an SDSS spectrum, we adopt the classification from NED if available.

In the right panel of Figure 8, we plot the DOGs and the control sample in the *WISE* color-color diagram. We mark several regions occupied by different types of objects (spirals, luminous infrared galaxies (LIRGs), and ULIRGs; see Figure 12 in Wright et al. 2010). We also overplot two AGN selection criteria proposed by Jarrett et al. (2011, solid lines) and Mateos et al. (2012, dashed lines). Most of the DOGs and the control sample are distributed in the region of LIRGs, confirming that they are IR luminous objects. The two AGN selection criteria are really efficient in selecting AGN-host

galaxies; most of the galaxies with a small AGN contribution (purple symbols) are outside the AGN selection boxes (see also Stern et al. 2012; Kirkpatrick et al. 2013 for other AGN criteria based on *WISE* colors).

4. COMPARISON OF LOCAL DOGS WITH THE CONTROL SAMPLE

To study how special the local analogs of DOGs are among MIR selected galaxies, we compare the physical properties of these DOGs with those of the control galaxy sample. We first compare UV and infrared properties in Section 4.1. We then discuss photometric/spectroscopic parameters and environments of DOGs in Sections 4.2 and 4.3, respectively.

4.1. Dust Obscuration in DOGs

To examine observational bias in our sample selection, we first show the flux density ratio between *WISE* 12 μm and *GALEX* NUV as a function of redshift in the

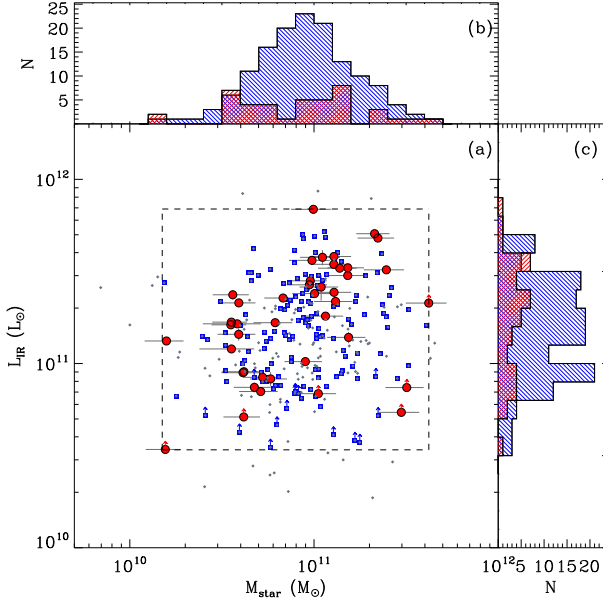


Figure 3. IR luminosity (L_{IR}) vs. stellar mass (M_{star}) for *WISE* 12 μm selected DOGs (red filled circles), the preliminary control sample of galaxies (gray diamonds) and the final control sample of galaxies (blue squares) (a). Dashed lines indicate the range of IR luminosity and stellar mass for *WISE* 12 μm selected DOGs. Arrows are lower limits to the IR luminosities (see Section 3.1). We plot error bars only for local DOGs. The histograms for IR luminosity (b) and stellar mass (c). DOGs and the final control sample are denoted by hatched histograms with orientation of 45° (// with red color) and of 315° (\\\ with blue color) relative to horizontal, respectively.

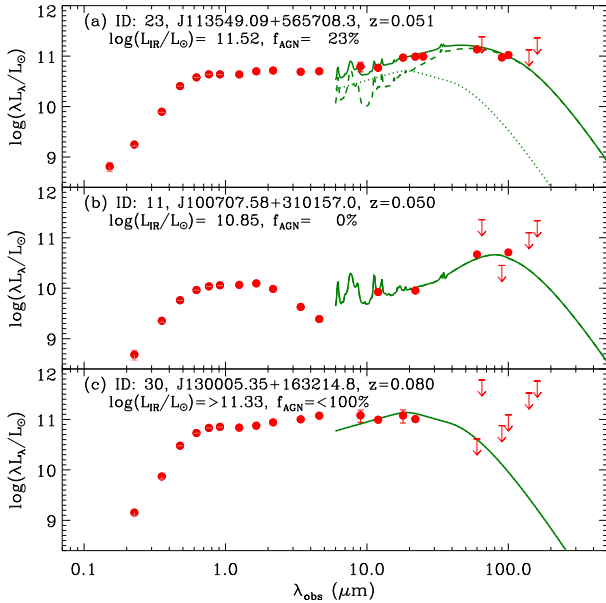


Figure 4. Example SEDs of FIR detected DOGs with some AGN contribution (a) and without an AGN contribution (b), and of an FIR undetected DOG (c). Filled circles are observed photometric data, and down arrows are upper limits. The detection limits for *IRAS* and *AKARI* can differ depending on the sky position. Therefore, the down arrows shown in these panels indicate just averaged upper limits. Solid, dotted, and dashed lines indicate the best-fit SEDs with the DECOMP routine of Mullaney et al. (2011), for total, host-galaxy, and AGN components, respectively.

top left panel of Figure 9. This flux density ratio is the one we use to select DOGs (see Figure 2). DOGs are indicated by circles, and the control sample is indicated by squares. We plot FIR detected and undetected galaxies with filled and open symbols, respectively. The figure indicates that the flux density ratio ($S_{12\mu\text{m}}/S_{0.22\mu\text{m}}$) shows no dependence either on the measured AGN contribution or on the FIR detection. However, the majority of FIR undetected galaxies (open symbols) have $z > 0.06$. This effect occurs simply because the FIR detection limit increases with redshift (see middle right panel). However, this redshift dependence does not introduce any bias in our results because both the DOGs and the control sample are affected in the same way.

The middle left panel shows the *WISE* 12 μm flux density as a function of redshift. The median flux densities of DOGs and the control sample are similar (36 ± 5 vs. 30 ± 2 mJy), but the dispersion is much larger for DOGs than for the control sample. There are some bright DOGs with $S_{12\mu\text{m}} > 100$ mJy. However, there are no such bright galaxies among the control sample even though there are initially some non-DOGs with $S_{12\mu\text{m}} > 100$ mJy in the top panel of Figure 2. Most relatively faint DOGs (e.g., $S_{12\mu\text{m}} < 40$ mJy) have a low AGN contribution (bluish symbols), but many bright DOGs contain a significant AGN contribution (green or red symbols). This result is similar to the one for high- z DOGs; bright 24 μm high- z DOGs are more AGN-dominated (Dey et al. 2008).

We note that high 12 μm flux densities do not necessarily imply high IR luminosities because IR luminosity estimates are more sensitive to FIR data and depend on detailed SED modeling. Thus we do not see any dependence of IR luminosity on AGN contribution for FIR detected galaxies (filled symbols) in the middle right panel. The middle right panel also shows that FIR undetected galaxies (open symbols) have lower IR luminosities than FIR detected galaxies (filled symbols), mainly as a result of the FIR detection limits.

The different AGN contribution among DOGs is more evident in the plot of flux density ratio between *IRAS* 60 μm and *WISE* 12 μm (bottom left panel). The control sample shows a scatter around the peak at a ratio of 20 (see blue histogram in (h)). However, the histogram of DOGs shows a clear bimodal distribution (red histogram in (h)). Most DOGs with a small AGN contribution (i.e., $f_{\text{AGN}} < 20\%$) have large $S_{60\mu\text{m}}/S_{12\mu\text{m}}$ (i.e., > 15); they are distributed in a range similar to the control sample. However, DOGs with a large AGN contribution have small $S_{60\mu\text{m}}/S_{12\mu\text{m}}$ (i.e., < 15). This bifurcation is also apparent for the flux density ratios between *IRAS* 100 μm and *WISE* 12 μm (not shown here). The presence of two types of DOGs in the local universe (i.e., DOGs with small $S_{60\mu\text{m}}/S_{12\mu\text{m}}$ and large AGN contribution vs. DOGs with large $S_{60\mu\text{m}}/S_{12\mu\text{m}}$ and small AGN contribution; see also middle left panel for $S_{12\mu\text{m}}$ in Figure 9) is similar to the situation for high- z DOGs; there are power-law (AGN-dominated and 24 μm bright) and bump (SF-dominated and 24 μm faint) DOGs (Dey et al. 2008).

The bottom right panel indicates that NUV magnitudes of DOGs are systematically fainter than for the control sample of galaxies. This difference suggests that the systematic UV faintness of DOGs is mainly responsible for the extreme ratios between *WISE* 12 μm and *GALEX* NUV flux densities. The NUV magnitude dis-

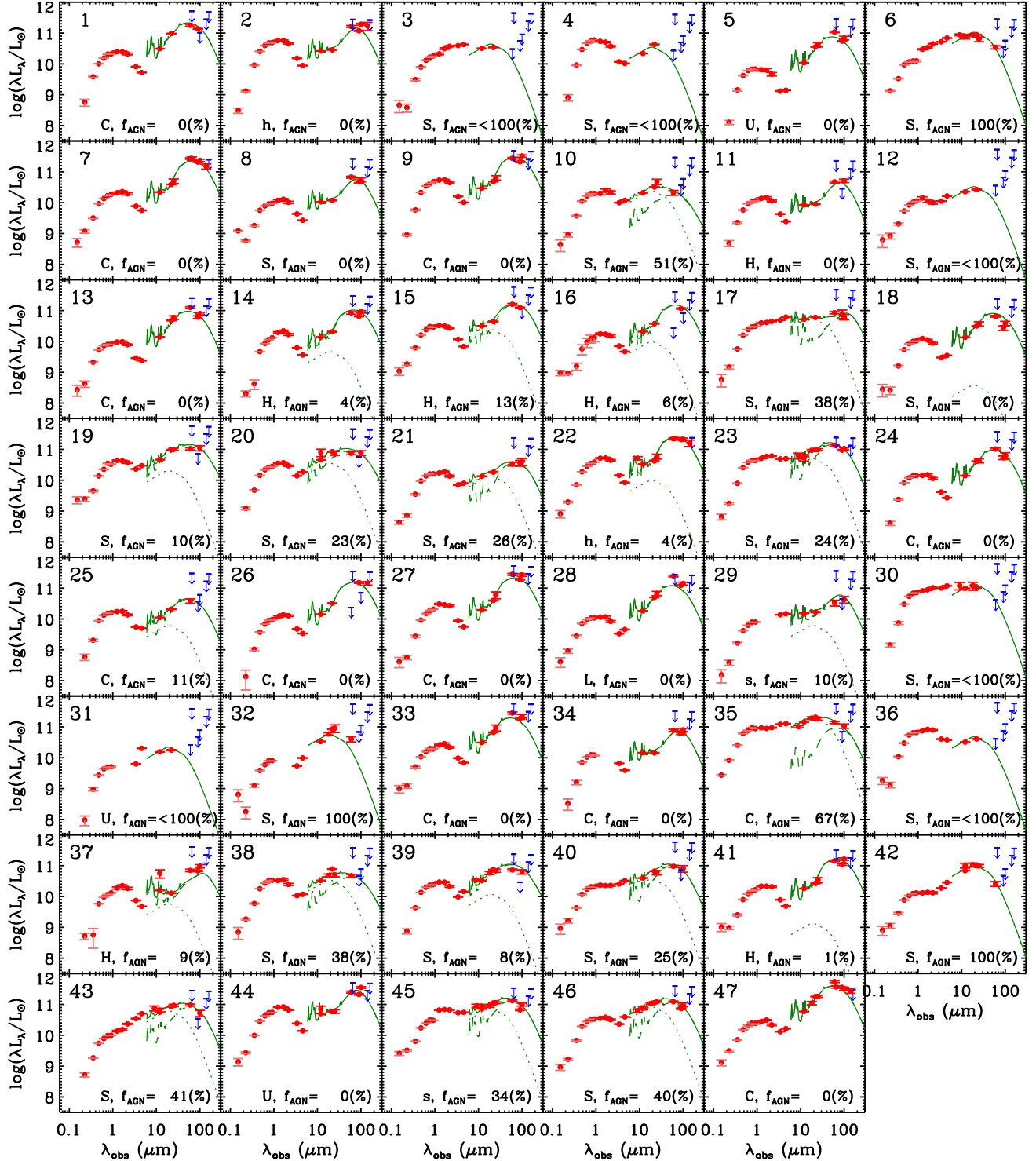


Figure 5. SEDs of 47 DOGs. Red filled circles are observed photometric data, and blue down arrows are upper limits. Solid, dotted, and dashed lines indicate the best-fit SEDs with the DECOMPIR routine of Mullaney et al. (2011), for total, host-galaxy, and AGN components, respectively. Number in the upper left corner of each panel is the identification in Table 1. Galaxy classification based on optical line ratios (H: SF, C: Composite, S: Seyfert, L: LINER, U: Undetermined) and the AGN contribution to the total IR luminosity are shown in the bottom of each panel. The lower case letter gives the classification adopted from NED.

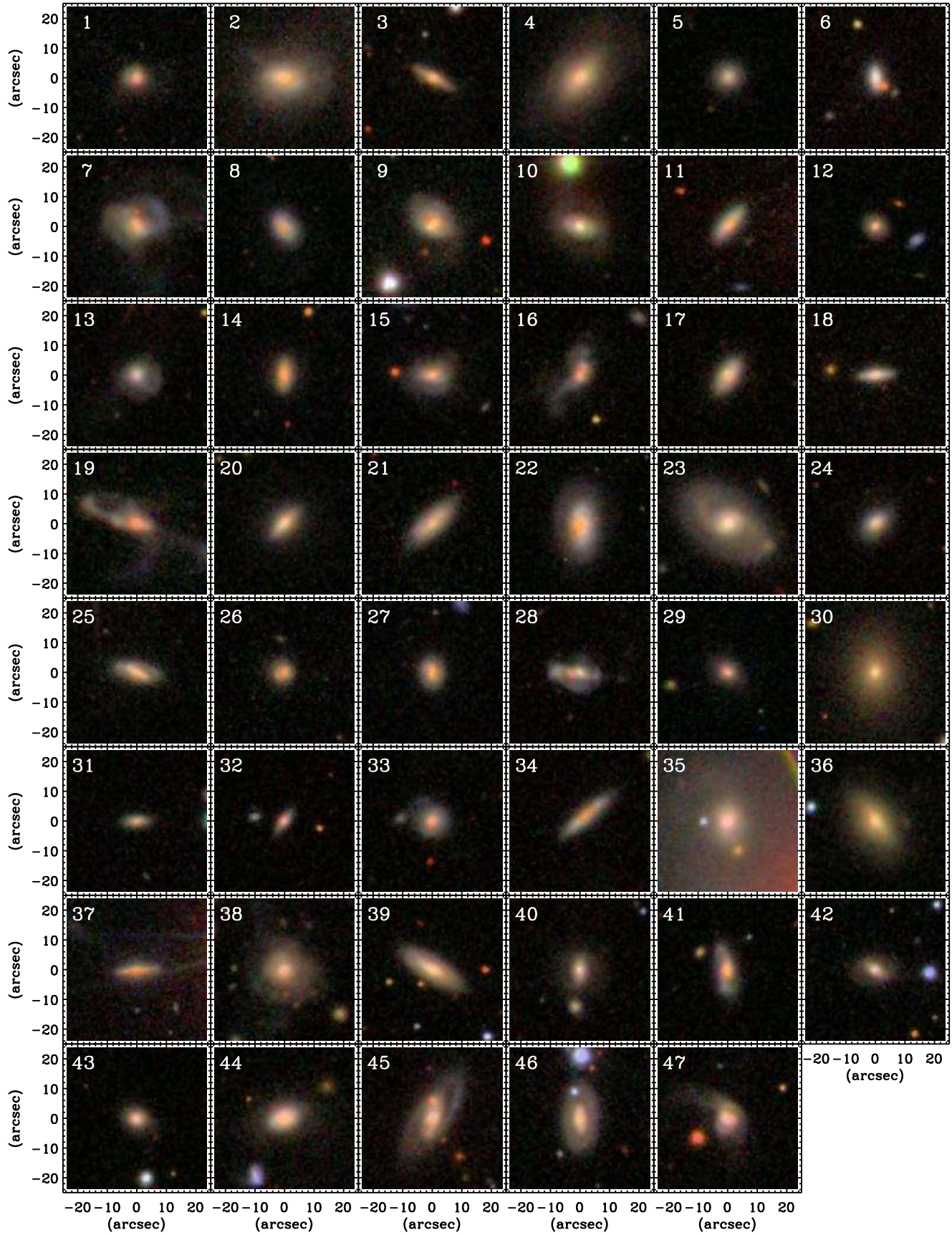


Figure 6. Optical color images ($50'' \times 50''$) of 47 DOGs (RGB color composites from *irg* bands). Number in the upper left corner of each panel is the identification in Table 1.

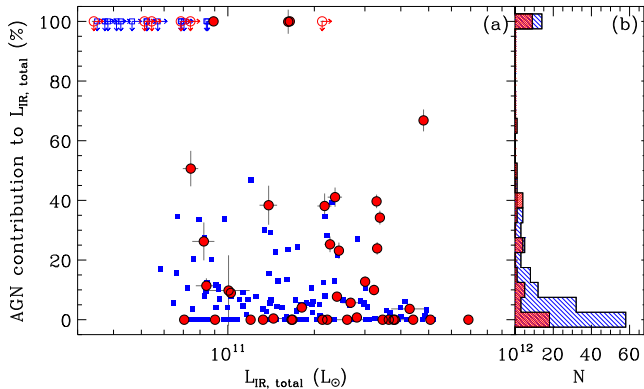


Figure 7. AGN contribution to the total IR luminosity as a function of total IR luminosity for DOGs (red circles) and the control sample (blue squares) (a), and its histogram (b). Filled and open symbols indicate FIR (i.e., *IRAS* 60 μm or *AKARI* 90 μm) detected and undetected galaxies, respectively. Arrows indicate lower and upper limits for the total IR luminosity and AGN contribution, respectively. We plot error bars only for local DOGs. DOGs and the control sample are denoted by hatched histograms with orientation of 45° (// with red color) and of 315° (\ \ with blue color) relative to horizontal, respectively.

tribution for DOGs with a large AGN contribution (e.g., $f_{\text{AGN}} \geq 20\%$) is the same as for those with a small AGN contribution (e.g., $f_{\text{AGN}} < 20\%$). A K-S test confirms this impression.

If one of the bands between *GALEX* NUV and *WISE* 12 μm is more important than the other band in explaining the extreme $S_{12\mu\text{m}}/S_{0.22\mu\text{m}}$, the distribution of DOGs should be significantly different from the control sample only in one panel. The middle left panel in Figure 9 shows that the flux density $S_{12\mu\text{m}}$ for DOGs is on average larger than for the control sample. The ratio of the medians of the two samples is 1.2. The K-S test also rejects the hypothesis that the $S_{12\mu\text{m}}$ distributions of the two samples are extracted from the same parent population with a confidence level of 99.8%. The bottom right panel shows that the flux density $S_{2.17\mu\text{m}}$ for the DOGs is again different from the control sample. The flux density ratio of the medians of the two samples is 5.8, much larger than for $S_{12\mu\text{m}}$.

This result indicates that both $S_{12\mu\text{m}}$ and $S_{0.22\mu\text{m}}$ are responsible for the extreme $S_{12\mu\text{m}}/S_{0.22\mu\text{m}}$ flux density ratio for DOGs. However, the larger difference in $S_{0.22\mu\text{m}}$ than for $S_{12\mu\text{m}}$ (i.e., factors of 5.8 vs. 1.2) strongly suggests that the UV faintness of DOGs is the main factor leading to the extreme $S_{12\mu\text{m}}/S_{0.22\mu\text{m}}$.

4.2. Optical Structure and Star Formation Activity of DOGs

We plot several photometric and spectroscopic parameters for the DOGs and for the control sample in Figure 10.

The top left panel shows *i*-band axis ratios of DOGs and the control sample. The ratio is the seeing-corrected *i*-band isophotal axis ratio adopted from the Korea Institute for Advanced Study (KIAS) VAGC¹⁰ (Choi et al. 2010). A K-S test for the axis ratio distributions of DOGs and the control sample rejects the hypothesis that the axis ratio distributions of the two samples are extracted from the same parent population with only a confidence

level of 88%. However, a Wilcoxon Rank-Sum test rejects the hypothesis that the two samples have the same mean with a confidence level of 96%. One interesting feature in this figure is that the fraction of DOGs with small axis ratios (e.g., ≤ 0.6) among DOGs is larger ($36 \pm 7\%$) than that among the control sample of galaxies ($17 \pm 3\%$). The large dust obscuration of some DOGs may simply result from the high inclination of disk galaxies (see also the color images in Figure 6).

We also plot *i*-band Petrosian radii of the DOGs (i.e., galaxy-size indicator) as a function of redshift in the top right panel. The Petrosian radius is adopted from the KIAS VAGC, calculated using elliptical annuli. This estimate is typically larger than the value based on circular annuli in the SDSS photometric database (Choi et al. 2007). The majority of DOGs are smaller than ~ 10 kpc; the control sample has a wider range of sizes. A K-S test rejects the hypothesis that the Petrosian radius distributions of the two samples are extracted from the same parent population with a confidence level of 99%. On the other hand, the K-S test for the distributions of Petrosian radii between DOGs with large and small AGN contribution (i.e., $f_{\text{AGN}} \geq 20\%$ vs. $f_{\text{AGN}} < 20\%$) indicates that the distributions of the two samples are not different.

The bottom left panel shows the flux ratios between $H\alpha$ and $H\beta$ (i.e., Balmer decrement) as a function of redshift. As expected, most DOGs and the control sample have $H\alpha/H\beta$ values larger than an intrinsic $H\alpha/H\beta$ ratio of 3.1 for AGN-dominated galaxies and $H\alpha/H\beta = 2.86$ for SF-dominated galaxies (in the nominal case B recombination for $T = 10,000$ K and $n_e \approx 10 \text{ cm}^{-3}$ with no dust, Osterbrock & Ferland 2006). Not surprisingly, the DOGs have on average larger values than the control sample. A K-S test supports this with a confidence level of 99.9%. The majority of DOGs with a small AGN contribution (purple symbols) have larger $H\alpha/H\beta$ values than the DOGs with a large AGN contribution (green and red symbols), suggesting that the DOGs with a small AGN contribution are more heavily obscured.

In bottom right panel, we compare sSFRs of DOGs with those of the control sample. We convert the IR luminosity (after removing the AGN contribution) into a SFR based on the relation in Kennicutt (1998) with the assumption of a Salpeter IMF: $\text{SFR} (M_{\odot} \text{ yr}^{-1}) = 1.72 \times 10^{-10} L_{\text{IR}} (L_{\odot})$. Note that we also use the Salpeter IMF for stellar mass estimates (see Section 2.3.2). The K-S test for DOGs and the control sample rejects the hypothesis that the sSFRs of the two samples are extracted from the same parent population with only a confidence level of 65%, indicating no significant difference between the two samples. The sSFRs of DOGs with a large AGN contribution (e.g., $f_{\text{AGN}} \geq 20\%$) tend to be smaller than those of DOGs with a small AGN contribution (e.g., $f_{\text{AGN}} < 20\%$). This conclusion is supported by the K-S test with a confidence level of 99%.

To compare the sSFRs of DOGs with the general trend for IR bright galaxies, we also plot FIR detected SDSS galaxies (gray dots) regardless of their 12 μm flux densities. The DOGs tend to have larger sSFRs than the FIR detected galaxies. This result is also confirmed by the K-S test that rejects the hypothesis that sSFRs of the two samples are extracted from the same parent population

¹⁰ <http://astro.kias.re.kr/vagc/dr7/>

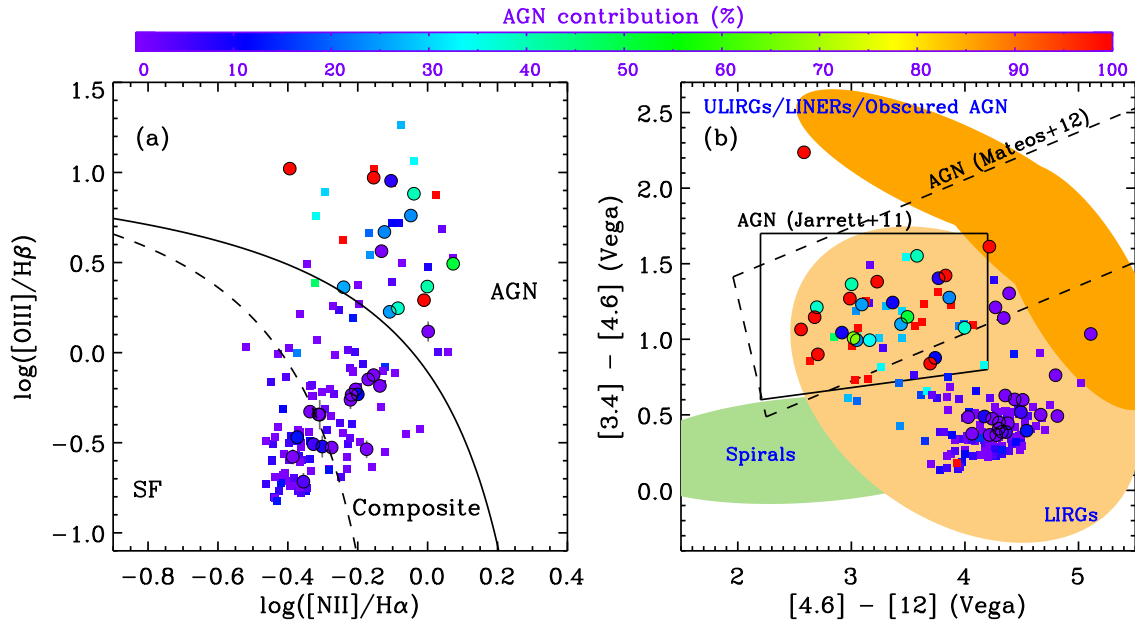


Figure 8. AGN diagnostic diagrams for DOGs based on optical [O III]/H β vs. [N II]/H α line ratios (a) and on *WISE* colors (b). Filled circles and squares indicate *WISE* 12 μ m selected DOGs and the control sample, respectively. Different colored symbols represent different AGN contributions measured from the SED decomposition (color coded as shown by the color bar to the top). We plot error bars only for local DOGs. Solid and dashed lines in (a) indicate the extreme starburst (Kewley et al. 2001) and pure SF limits (Kauffmann et al. 2003b), respectively. Solid and dashed lines in (b) are the MIR AGN selection criteria proposed by Jarrett et al. (2011) and Mateos et al. (2012), respectively. We mark several regions occupied by different classes of objects (spirals, LIRGs and ULIRGs; see Figure 12 in Wright et al. 2010).

with a confidence level of 99.9%. However, the median sSFRs of DOGs and the control sample are larger than those of FIR detected galaxies by only a factor $\lesssim 2$, suggesting that the star formation modes of DOGs and the control sample are not significantly different from typical IR bright galaxies. In other words, the small difference in sSFRs between DOGs and FIR detected galaxies indicates that most DOGs are not starburst systems with much larger (i.e., factors > 2) sSFRs than typical IR bright galaxies (Elbaz et al. 2011).

4.3. Large- and Small-scale Environments of DOGs

Because star formation or nuclear activity of galaxies is strongly related to their environment (e.g., Park & Choi 2009; Blanton & Moustakas 2009; Hwang et al. 2012c), we next compare the environments of DOGs with those of the control sample. Here we consider two environmental indicators: a surface galaxy number density estimated from the five nearest neighbor galaxies (Σ_5) as a large-scale environmental parameter, and a distance to the nearest neighbor galaxy (R_n) as a small-scale environmental parameter.

The background density, Σ_5 , is defined by $\Sigma_5 = 5(\pi D_{p,5}^2)^{-1}$, where $D_{p,5}$ is the projected distance to the 5th-nearest neighbor. The fifth-nearest neighbor to each target galaxy is identified in a volume-limited sample ($0.05 < z < 0.08$ and $M_r \leq -19.94$, dashed line in the top left panel of Figure 11) among the neighbor galaxies that have relative velocities $\Delta v = |v_{\text{neighbors}} - v_{\text{target}}| < 1500 \text{ km s}^{-1}$ to exclude foreground and background galaxies.

To define the small-scale environmental parameter attributed to the nearest neighbor, we first search for the nearest neighbor of a target galaxy that is the closest to the target galaxy projected on the sky and that satis-

fies conditions on magnitude and relative velocity. We search for the nearest neighbor galaxy among galaxies with magnitudes brighter than $M_r = M_{r,\text{target}} + 0.5$ and with relative velocities less than $\Delta v = 600 \text{ km s}^{-1}$ for early-type target galaxies and less than $\Delta v = 400 \text{ km s}^{-1}$ for late-type target galaxies. These velocity limits cover most close neighbors including dusty star-forming galaxies in the local universe (see Figure 2 of Barton et al. 2000 and Figure 1 of Park et al. 2008). The magnitude criterion selects galaxies mostly in major interacting pairs; these objects should be the most effective in triggering SFA (Woods & Geller 2007; Cox et al. 2008; Hwang et al. 2010a). To have a fair sample of neighbor galaxies in our sample, we select target galaxies among those with $M_{r,\text{target}} = -19.94 - 0.5$ where $M_r \leq -19.94$ is the magnitude limit of the volume-limited sample (see top left panel in Figure 11).

The top left panel of Figure 11 shows the *r*-band absolute magnitudes of DOGs (circles) and the control sample (squares). For comparison, we also plot the FIR detected SDSS galaxies (gray dots). The distribution of DOGs does not differ from FIR detected galaxies. However, the DOGs tend to be fainter than the control sample, confirmed by a K-S test with a confidence level of 99.9%. The distributions of redshift and stellar mass for DOGs and the control sample are similar (see Figure 3). Thus, the different *r*-band absolute magnitude distributions simply reflect the difference in the amount of dust extinction; DOGs are more dust obscured by definition. Thus, they are optically fainter than the control sample.

The top right panel shows Σ_5 distributions of DOGs, the control sample, and FIR detected SDSS galaxies as a function of stellar mass. The Σ_5 distribution of DOGs does not differ from the control sample or from the FIR detected galaxies, as confirmed by a K-S test. FIR de-

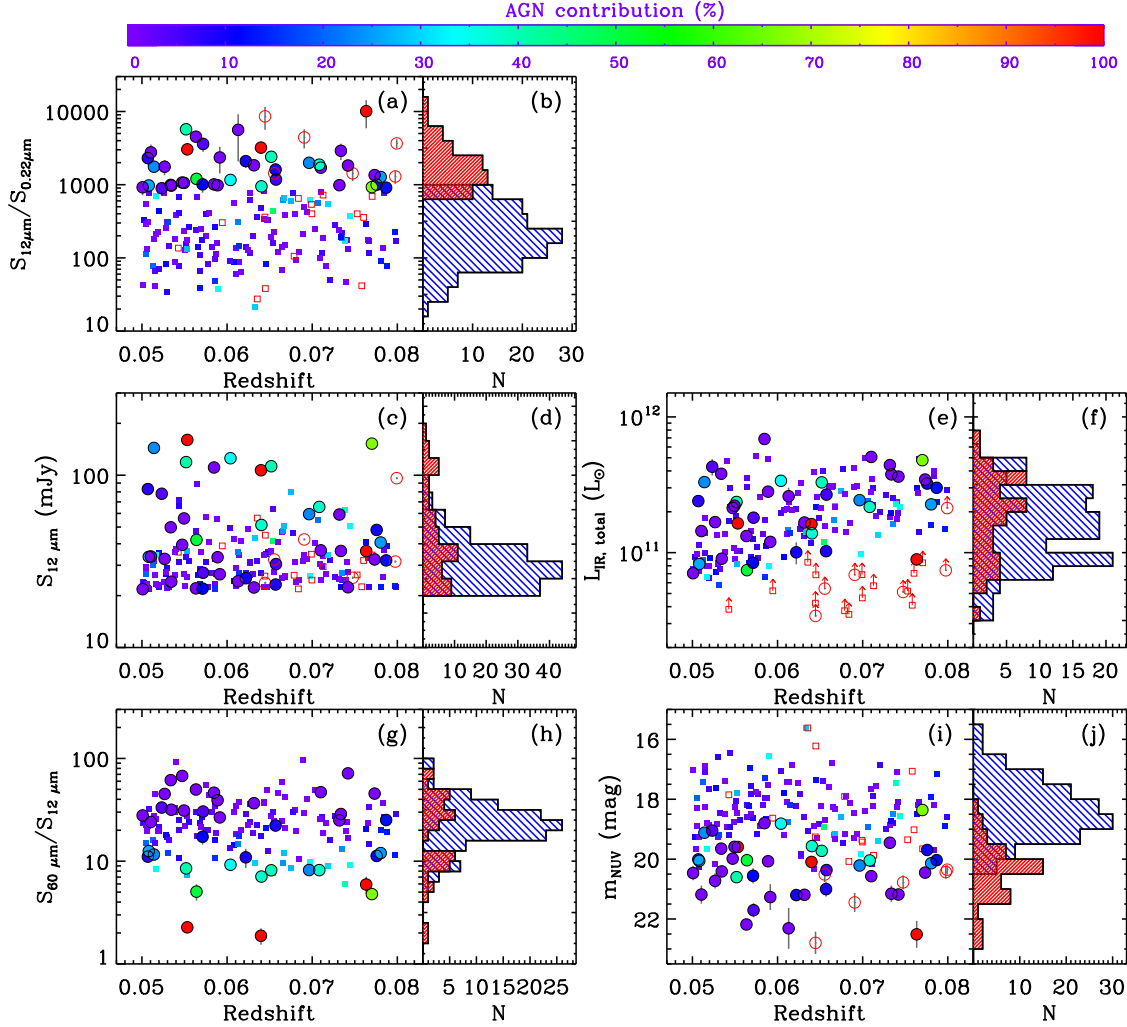


Figure 9. Flux density ratios between *WISE* 12 μm and *GALEX* NUV for local DOGs (circles) and for the control sample (squares) as a function of redshift (a), and their histograms (b). Filled and open symbols indicate FIR (i.e., *IRAS* 60 μm or *AKARI* 90 μm) detected and undetected galaxies, respectively. Different colored symbols represent different AGN contributions measured from the SED decomposition (color coded as shown by the color bar to the top). We plot error bars only for local DOGs. DOGs and the control sample are denoted by hatched histograms with orientation of 45° (// with red color) and of 315° (\ \ with blue color) relative to horizontal, respectively. Same as (a-b), but for *WISE* 12 μm flux density (c-d), for total IR luminosity (e-f), for flux density ratios between *IRAS* 60 μm and *WISE* 12 μm (g-h), and for NUV magnitude (i-j). Arrows in (e) indicate lower limits to the total IR luminosities.

tected galaxies are usually absent in high-density regions in the local universe because galaxies in these regions have lost (or consumed) the gas/dust, necessary for their IR activity (Hwang et al. 2010a). DOGs and the control sample, similar to FIR detected galaxies, are also mostly located in low-density regions.

The Σ_5 distribution of DOGs with a large AGN contribution (e.g., $f_{\text{AGN}} \geq 20\%$) is similar to those with a small AGN contribution (e.g., $f_{\text{AGN}} < 20\%$). Although there are two DOGs in relatively high-density regions (e.g., $\Sigma_5 > 6 \text{ Mpc}^{-2}$) and both of them have a large AGN contribution, the K-S test cannot reject the hypothesis that the Σ_5 distributions of the two samples are extracted from the same parent population (but see Brodwin et al. 2008 for stronger clustering for bright (probably more AGN-dominated) DOGs at $z \sim 2$).

In the bottom panels, we plot the projected distance to the nearest neighbor galaxy of DOGs as a function of their stellar mass. Because galaxy properties are strongly correlated with the morphological type of the near-

est neighbor galaxy (Park & Choi 2009; Hwang et al. 2010a), we plot the distribution of neighbor separation separately according to their neighbor’s morphology: late-type neighbor case (bottom left panel) and early-type neighbor case (bottom right panel). We adopt galaxy morphology data from the KIAS VAGC.

The bottom panels show that there are more close pairs (e.g., $R_n < 0.1 \text{ Mpc}$) for the late-type neighbor case (bottom left panel) than for the early-type neighbor case (bottom right panel). This is true for all the samples (DOGs, control sample and FIR detected galaxies), confirming the dependence of IR activity of dusty galaxies on the morphological type (i.e., cold gas fraction) of the nearest neighbor galaxy (Hwang et al. 2010a). Moreover, both panels show that the majority of DOGs have neighbor separation $R_n \gtrsim 0.3 \text{ Mpc}$, indicating that the majority of DOGs are not currently interacting galaxies. However, it does not necessarily imply that galaxies with large pair separation are currently quiescent systems (see Section 6 for details). The neighbor separation distribu-

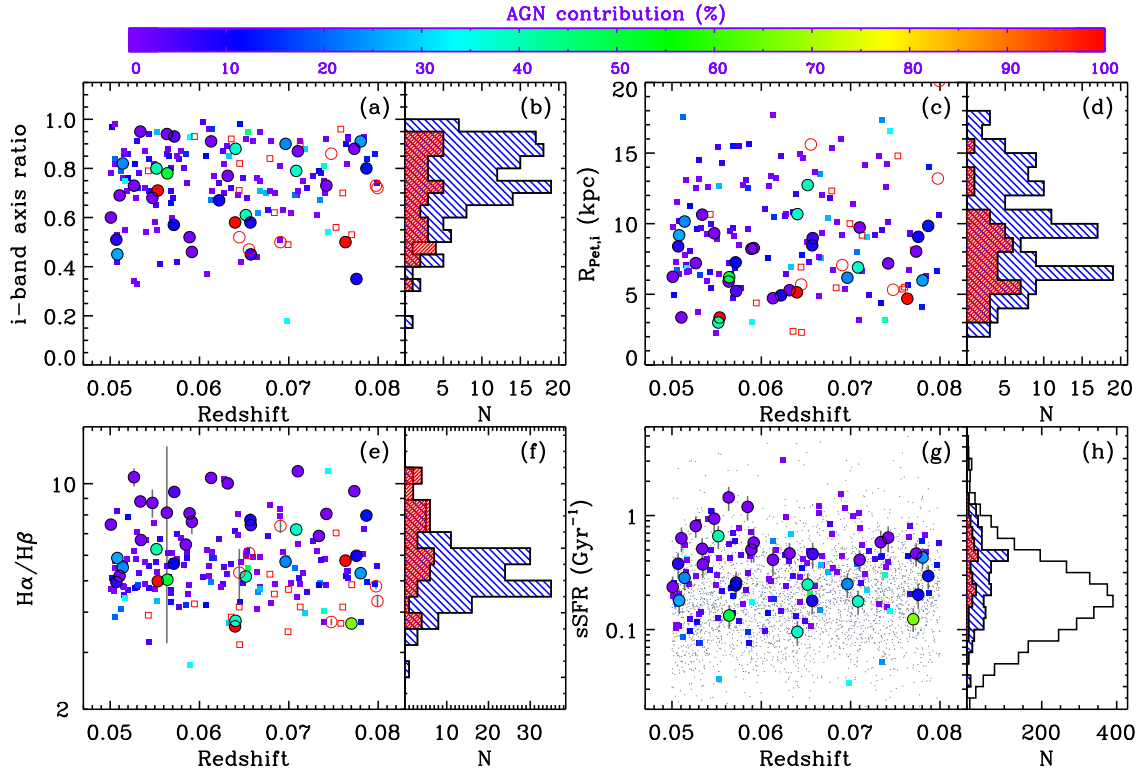


Figure 10. Same as Figure 9, but for i -band axis ratio (a-b), i -band Petrosian radius (c-d), Balmer decrement ($H\alpha/H\beta$) (e-f), and sSFRs (g-h). We plot error bars only for local DOGs in (e) and (g). In (g-h), FIR detected galaxies are shown as gray dots and as an open histogram. To better show the histograms in (h), we multiply the histograms of DOGs and the control sample of galaxies by five.

tion of DOGs does not differ from the control sample or from the FIR detected galaxies.

5. COMPARISON OF LOCAL AND HIGH-Z DOGS

Because of the limited observational data for SDSS galaxies, the selection criteria for the local DOGs are not exactly identical to those of high- z DOGs. However, both local and high- z DOGs have extreme flux density ratios between rest-frame MIR and UV. These local DOGs are reasonable local analogs of high- z DOGs. In this section, we compare physical properties of local and high- z DOGs.

Before we compare local DOGs with high- z ones, we emphasize that the IR luminosities of current samples of local and high- z DOGs differ. The high- z DOGs we discuss are mainly from Dey et al. (2008) who identified ~ 2600 DOGs with $S_{24\mu\text{m}} \geq 300 \mu\text{Jy}$ in the NOAO Deep Wide-Field Survey Boötes field, from Sajina et al. (2012) who identified 26 DOGs with $S_{24\mu\text{m}} \geq 890 \mu\text{Jy}$ in the *Spitzer* Extragalactic First Look Survey field¹¹, and from Penner et al. (2012) who identified ~ 60 DOGs with $S_{24\mu\text{m}} \geq 53 \mu\text{Jy}$ in the Great Observatories Origins Deep Survey (GOODS). Although the stellar masses of local and high- z DOGs are similar, the IR luminosities of most high- z DOGs exceed $10^{12} L_{\odot}$ (i.e., ULIRGs) simply because of the detection limits (Bussmann et al. 2012; Melbourne et al. 2012; Sajina et al. 2012; Penner et al. 2012). However, the IR luminosities of local DOGs are an order of magnitude lower than for the high- z DOGs (see Figure 3). We keep this luminosity difference between the two samples in mind for the following analysis.

¹¹ <http://ssc.spitzer.caltech.edu/fls/>

It should also be noted that the universe at $z \sim 2$ differs from that at $z \sim 0$. The main relevant difference is the gas (or dust) fraction in galaxies (Daddi et al. 2010b; Tacconi et al. 2010; Magdis et al. 2012; Sargent et al. 2013). Because the gas fraction in galaxies at $z \sim 2$ is greater than for at $z \sim 0$ (also dust), galaxies at $z \sim 2$ can more easily be IR luminous than those at $z \sim 0$ without invoking galaxy-galaxy interactions or mergers (Daddi et al. 2010a; Elbaz et al. 2011).

5.1. The AGN Contribution in DOGs

Among many similarities between local and high- z DOGs, the most striking is that both have two subclasses: AGN- and SF-dominated DOGs. For example, high- z DOGs are usually grouped into two classes based on their rest-frame NIR/MIR SEDs; there are bump and power-law DOGs (Dey et al. 2008). Power-law DOGs are relatively bright at $24 \mu\text{m}$, and contain an AGN dust component in contrast with bump DOGs. Similarly, local DOGs can be divided into two classes. The local DOGs with a large AGN contribution are bright at $12 \mu\text{m}$. They also contain an AGN dust component similar to power-law high- z DOGs (see middle left and bottom left panels in Figure 9).

Secondly, the sSFRs of local DOGs with a small AGN contribution are larger than those with a large AGN contribution (see bottom right panel in Figure 10). Melbourne et al. (2012) found a similar result for high- z DOGs. They use IR8 value ($\equiv L_{\text{IR}}/\nu L_{\nu}(8 \mu\text{m})$), a good proxy for sSFRs of IR bright galaxies in a given redshift (Elbaz et al. 2011), as the basis for their conclusion.

Another interesting comparison is that galaxy size might depend on the AGN contribution. For high-

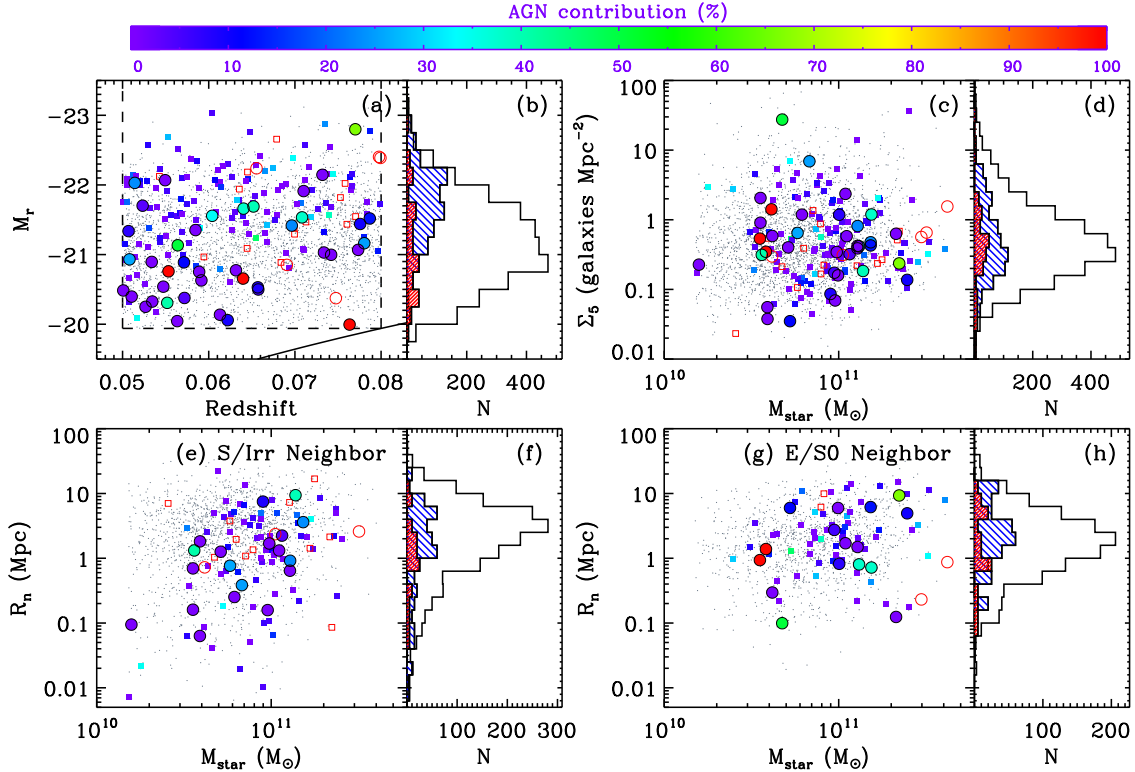


Figure 11. Same as Figure 9, but for r -band absolute magnitude (a-b), surface galaxy number density (Σ_5) (c-d), distance to the nearest neighbor galaxy for late-type neighbor case (e-f) and for early-type neighbor case (g-h). Environmental parameters in panels (c, e and g) are plotted as a function of stellar mass. FIR detected galaxies are shown as gray dots and as an open histogram. Dashed lines in (a) define the volume-limited sample. The bottom solid curve corresponds to the apparent magnitude limit ($m_r = 17.77$) for the main galaxy sample in SDSS (Choi et al. 2007). To better show the histograms, we multiply the histograms of DOGs and the control sample of galaxies by five.

z DOGs, some studies suggest that power-law objects tend to be smaller and more concentrated than bump objects (Melbourne et al. 2009; Donley et al. 2010; Bussmann et al. 2009a, 2011). However, the top right panel in Figure 10 suggests no size difference between local DOGs with small and large AGN contribution. It is interesting to note that Bussmann et al. (2011) found similar sizes for high- z bump and power-law DOGs when they considered only the objects with $H < 22.5$ (mag). Recent deep, near-infrared surveys using *HST* Wide Field Camera 3 (WFC3) including the Cosmic Assembly Near-Infrared Dark Energy Legacy Survey (CANDELS; Grogin et al. 2011) will be useful for resolving this issue by increasing the statistics for high- z DOGs.

5.2. Dust Obscuration of Local and High- z DOGs

Both local and high- z DOGs are, by definition, galaxies with large dust obscuration that also affects their optical spectra. The Balmer decrement of local DOGs is in the range $H\alpha/H\beta \approx 3.6-11$ (see bottom left panel in Figure 10), equivalent to $A(H\alpha) \approx 0.7-3.8$ if we assume the Calzetti et al. (2000) extinction curve and the intrinsic ratio of $H\alpha/H\beta \approx 2.86$ (case B recombination for $T = 10,000$ K and $n_e \approx 10 \text{ cm}^{-3}$ with no dust; Osterbrock & Ferland 2006). These amounts of extinction are slightly smaller than those of high- z DOGs (e.g., $A(H\alpha) \approx 2.4-4.6$ for three high- z DOGs, see Brand et al. 2007). However, the amount of dust extinction can depend on IR luminosity. Therefore, it is not clear whether this difference in the amount of dust extinction between

local and high- z DOGs results from evolution in dust properties or from different IR luminosities.

To distinguish these two effects, we plot the ratio between $H\alpha$ and IR luminosities of DOGs ($L_{H\alpha, \text{uncorr}}/L_{\text{IR, total}}$) as a function of IR luminosity in Figure 12. Because the Balmer decrement is not available for many high- z DOGs, we use $L_{H\alpha, \text{uncorr}}/L_{\text{IR, total}}$ as a proxy for dust extinction. Here $L_{H\alpha, \text{uncorr}}$ is the observed $H\alpha$ luminosity after aperture correction, but without any dust-extinction correction. To compare the behavior of DOGs with the general trend for IR bright galaxies, we also plot the FIR detected SDSS galaxies (gray dots).

One interesting feature in Figure 12 is that $L_{H\alpha, \text{uncorr}}/L_{\text{IR, total}}$ of galaxies decreases (i.e., more extinguished) with increasing IR luminosity. As expected, $L_{H\alpha, \text{uncorr}}/L_{\text{IR, total}}$ of local DOGs (filled circles) is smaller (i.e., more extinguished) than for the control sample (filled squares) or for the FIR detected galaxies (gray dots). On the other hand, $L_{H\alpha, \text{uncorr}}/L_{\text{IR, total}}$ of local DOGs (filled circles) is larger (i.e., less extinguished) than for high- z DOGs (filled triangles). Because there are no local DOGs in the same IR luminosity range as high- z DOGs, it is difficult to tell whether the difference in $L_{H\alpha, \text{uncorr}}/L_{\text{IR, total}}$ between local and high- z DOGs results from evolution in dust properties or from different IR luminosities. However, FIR detected galaxies at $L_{\text{IR, total}} > 10^{12} (L_{\odot})$ seem to be smoothly connected to high- z DOGs (filled triangles), suggesting that the difference in $L_{H\alpha, \text{uncorr}}/L_{\text{IR, total}}$ between local and high-

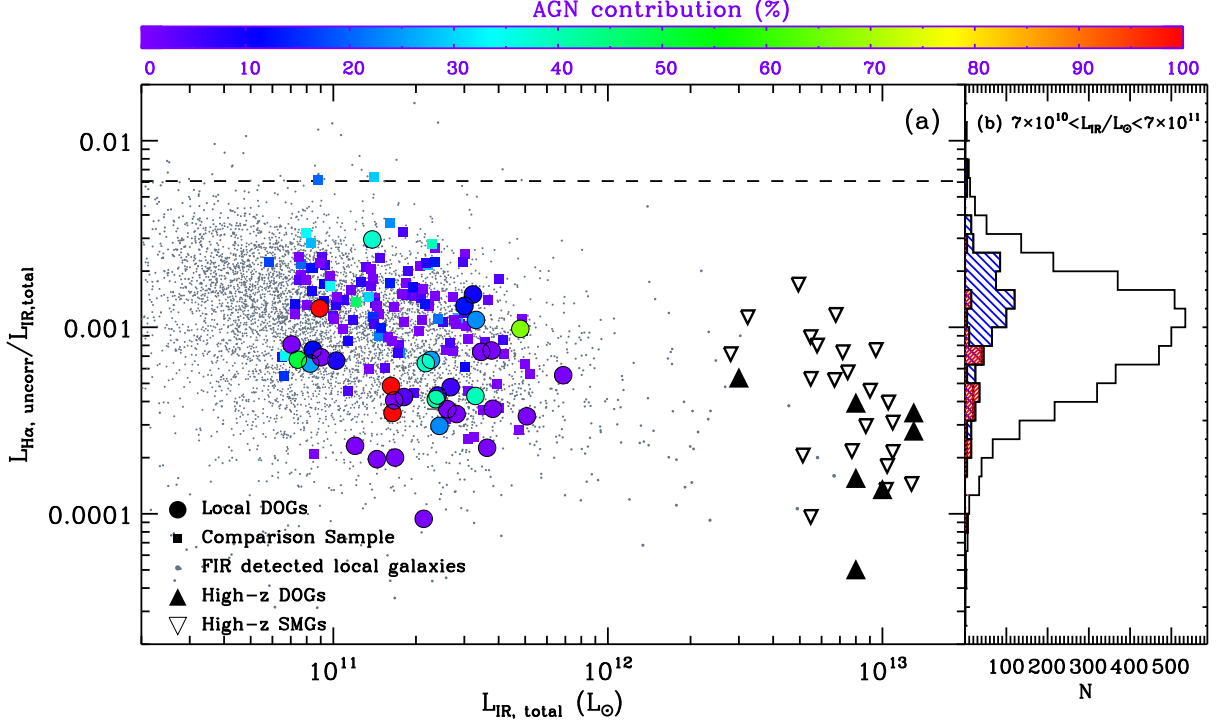


Figure 12. $L_{\text{H}\alpha, \text{uncorr}}/L_{\text{IR, total}}$ vs. $L_{\text{IR, total}}$ for local DOGs (circles) and the control sample (squares) (a), and their histograms (b). $L_{\text{H}\alpha, \text{uncorr}}$ is observed H α luminosity after aperture correction, but without dust-extinction correction. Different colored symbols represent different AGN contributions measured from the SED decomposition (color coded as shown by the color bar to the top). We plot error bars only for local DOGs (not visible because of large symbols). For comparison, we also plot the FIR detected SDSS galaxies at $z > 0.05$ (gray dots), high- z DOGs (filled triangles, Brand et al. 2007) and SMGs (open upside down triangles, Swinbank et al. 2004). Dashed line indicates when H α and $L_{\text{IR, total}}$ SFR indicators would agree. To have a fair comparison in (b), we use only galaxies at $7 \times 10^{10} < L_{\text{IR, total}}/L_{\odot} < 7 \times 10^{11}$. Local DOGs and the control sample are denoted by hatched histograms with orientation of 45° (// with red color) and of 315° (\ \ with blue color) relative to horizontal, respectively. The open histogram refers to FIR detected SDSS galaxies. To better show the histograms, we multiply the histograms of local DOGs and the control sample by five.

z DOGs results mainly from different IR luminosities rather than from evolution in dust properties. Interestingly, the $L_{\text{H}\alpha, \text{uncorr}}/L_{\text{IR, total}}$ distribution of local DOGs (filled circles) is similar to that for submillimeter galaxies at $z \sim 2$ (open upside down triangles, Swinbank et al. 2004), even though their IR luminosities differ by more than an order of magnitude.

5.3. Dust Temperature of Local and High- z DOGs

To further compare the dust properties of local and high- z DOGs, we plot their dust temperature as a function of IR luminosity in Figure 13. We estimate the dust temperature of our sample galaxies including local DOGs (filled circles), the control sample (filled squares), and FIR detected SDSS galaxies (gray dots) by converting the flux density ratio of *IRAS* 60 μm and 100 μm into a dust temperature. We use the following conversion equation, originally derived in Hwang et al. (2011):

$$T_{\text{dust}} \text{ (K)} = (43.0 \pm 0.3) + (37.0 \pm 1.5) \log(S_{60\mu\text{m}}/S_{100\mu\text{m}}). \quad (1)$$

Hwang et al. derived this conversion equation by comparing the *IRAS* 60/100 μm flux density ratio with the dust temperature directly measured from the SED fit of *AKARI* 140 or 160 μm detected SDSS galaxies. They fit the observational data with a modified black body model and fix the emissivity parameter to $\beta = 1.5$ (see Hwang et al. 2010b; Elbaz et al. 2010 for more details).

As expected, Figure 13 shows that the dust temperature of local galaxies including DOGs, control sample,

and FIR detected galaxies increases with increasing IR luminosity (Chapman et al. 2003; Hwang et al. 2010b; Amblard et al. 2010). These galaxies are smoothly connected to the region occupied by ULIRGs at $0.1 \lesssim z \lesssim 3.0$ (pink region). In a given IR luminosity range (e.g., $7 \times 10^{11} < L_{\text{IR, total}}/L_{\odot} < 7 \times 10^{12}$ where local DOGs exist), the dust temperature of local DOGs (see red histogram in the right panel) is on average higher than for the control sample and for the FIR detected galaxies.

Most high- z DOGs in Melbourne et al. (2012, filled triangles) and Sajina et al. (2012, open triangles) have dust temperatures similar to or lower than local DOGs, even though the IR luminosities of high- z DOGs are much higher than those of local DOGs. Moreover, the majority of high- z DOGs follow the trend of high- z submillimeter galaxies (SMGs, blue region), but have much lower dust temperature than ULIRGs at $L_{\text{IR, total}}/L_{\odot} \sim 10^{12}$.

These data suggest that high- z DOGs have dust temperature similar to or lower than other IR bright galaxies at similar redshift. However, the dust temperature of high- z DOGs is measured only for those detected both at 250 μm and 350 μm (Melbourne et al. 2012; Sajina et al. 2012). DOGs not detected in these bands (i.e., many DOGs with high dust temperature) are unlikely to appear in this plot. Moreover, blending issue in the photometry of these *Herschel* 250–500 μm bands can also introduce a systematic bias toward lower dust temperature estimates (Hwang et al. 2010b; R. Leiton et al. 2013, in preparation).

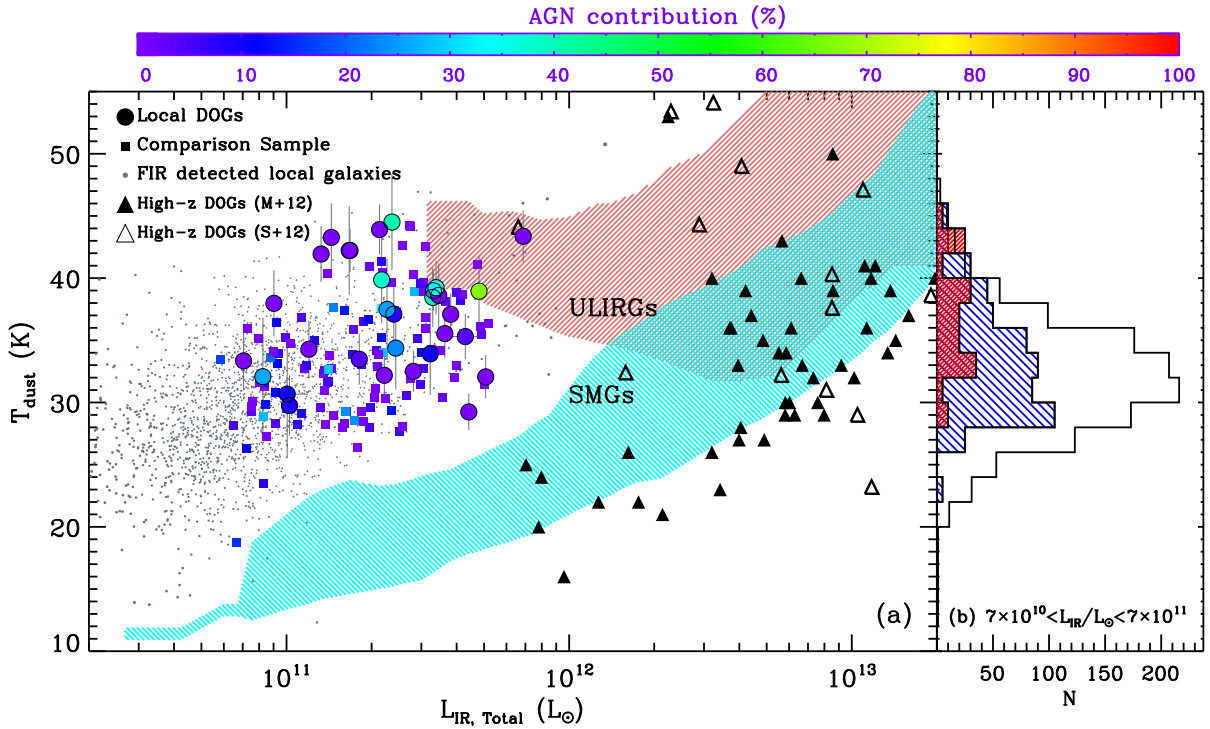


Figure 13. Dust temperature vs. total IR luminosity for local DOGs (circles) and for the control sample (squares) (a), and their histograms (b). Different colored symbols represent different AGN contributions measured from the SED decomposition (color coded as shown by the color bar to the top). We plot error bars only for local DOGs. For comparison, we also plot FIR detected SDSS galaxies at the same redshift range as local DOGs (i.e., $0.05 < z < 0.08$, gray dots), and high- z DOGs (filled triangles from Melbourne et al. 2012 and open triangles from Sajina et al. 2012). The loci of ULIRGs at $0.1 \lesssim z \lesssim 3$ (Yang et al. 2007; Younger et al. 2009; Magdis et al. 2010) and high- z SMGs (Chapman et al. 2005; Kovács et al. 2006; Magnelli et al. 2012) are shown as regions filled by pink and blue color, respectively. To have a fair comparison in (b), we use only galaxies at $7 \times 10^{10} < L_{\text{IR, total}}/L_{\odot} < 7 \times 10^{11}$. Local DOGs and the control sample are denoted by hatched histograms with orientation of 45° (// with red color) and of 315° (\ \ with blue color) relative to horizontal, respectively. The open histogram refers to FIR detected local galaxies. To better show the histograms, we multiply the histograms of local DOGs and the control sample by five.

The lack of high- z DOGs with high dust temperature at $L_{\text{IR, total}}/L_{\odot} \sim 10^{12}$ could result simply from selection effects (see also discussion in Melbourne et al. 2012 and their Figure 10). This issue, especially for high- z IR bright galaxies, is examined well in Magdis et al. (2010), Chapin et al. (2011) and Symeonidis et al. (2013). The detection of some high- z DOGs with high dust temperature (e.g., $T_{\text{dust}} \gtrsim 60$ K with $L_{\text{IR}}/L_{\odot} > 10^{13}$) among *WISE* selected galaxies demonstrates that they do exist (Wu et al. 2012; there are also some in Sajina et al. 2012).

6. DISCUSSION: DIVERSE NATURE OF LOCAL AND HIGH- Z DOGS

There are apparently two types of local DOGs with small and large AGN contribution to their IR luminosities; high- z DOGs show the same two populations. The bottom left panel in Figure 9 shows that the flux density ratios between *IRAS* $60 \mu\text{m}$ and *WISE* $12 \mu\text{m}$ are systematically smaller for local DOGs with a large AGN contribution than those with a small AGN contribution. This trend is also apparent for high- z DOGs (i.e., power-law DOGs vs. bump DOGs), even though the observed bands are not identical (e.g., see Figure 7 in Melbourne et al. 2012 for the flux density ratio of $S_{250\mu\text{m}}/S_{24\mu\text{m}}$ for $z \sim 2$ DOGs). Because rest-frame $60\text{--}100 \mu\text{m}$ data are closely related to the total IR luminosities of dusty galaxies and $12 \mu\text{m}$ data are sensitive to a hot AGN dust component, a smaller flux density ratio

between FIR and MIR bands for a smaller AGN contribution is consistent with expectation (Veilleux et al. 2009; Mullaney et al. 2011; Kirkpatrick et al. 2012).

The main reason for the extreme $S_{12\mu\text{m}}/S_{0.22\mu\text{m}}$ flux density ratios in local DOGs is the abnormal faintness in the NUV rather than the extreme brightness at $12 \mu\text{m}$ (see middle left ($S_{12\mu\text{m}}$) and bottom right ($S_{0.22\mu\text{m}}$) panels in Figure 9). This result is also valid for AGN-dominated DOGs. This result is supported by the larger $H\alpha/H\beta$ flux ratios (i.e., Balmer decrement) of local DOGs relative to the control sample.

The abnormal faintness in the NUV we find for local DOGs is consistent with the conclusion for high- z DOGs (Penner et al. 2012). Penner et al. further suggest that the large dust obscuration in DOGs could result from the spatial coincidence between dust and massive stars or from a large dust content. In both cases, merging process between galaxies that can significantly change the dust geometry or galaxy inclination can play an important role. Simulations also suggest that bright DOGs are recent merger products, but fainter DOGs could have a diverse origin including the large inclination of disk galaxies (Narayanan et al. 2010). The optical color images of local DOGs in Figure 6 indeed show that there are some galaxies in the process of merging (e.g., ID: 7, 13, 16, 19, 47; see also Melbourne et al. 2009; Donley et al. 2010; Busmann et al. 2011 for high- z DOGs with merging features).

The larger fraction of galaxies with small axis ratios

(< 0.6) among local DOGs than that among the control sample of galaxies (i.e., $36 \pm 7\%$ for DOGs, but $17 \pm 3\%$ for control sample; see top left panel in Figure 10 and color images in Figure 6) and the large pair separation for local DOGs (see bottom panels in Figure 11) suggest that the large dust obscuration of some DOGs simply results from their large inclination. The optical color images of our local DOGs in Figure 6 confirm that some DOGs are indeed highly-inclined disk galaxies (e.g., ID: 3, 11, 21, 34, 37). However, it should be noted that galaxies with large pair separation do not necessarily imply that they are currently quiescent systems. When two galaxies have just finished merging, the new nearest neighbor galaxy of the merger product may be far away. Therefore, some DOGs with large pair separation (e.g., $R_n \gtrsim 0.3$ Mpc) could be recent merger remnants (or late stage mergers). Actually, Park et al. (2008) showed that, at fixed background density, postmerger features including large displacement of the galaxy nucleus from the center, turmoil features, and/or very close double cores, are more frequently seen in the isolated galaxies than less isolated ones. The optical color images in Figure 6 show some of these cases for local DOGs, but the fraction of these systems is not large.

High resolution optical images for high- z DOGs also suggest that many DOGs are undisturbed disk galaxies rather than merging objects (Kartaltepe et al. 2012; Schawinski et al. 2012). Simulations by Narayanan et al. (2010) also show that isolated disk galaxies can satisfy DOG selection criteria when they are edge-on. It is also interesting that half or more of local DOGs have neither small axis ratios (i.e., edge-on systems) nor obvious signs of galaxy-galaxy interactions and mergers (e.g., ID: 5, 27, 30, 36, 43).

These results suggest both local and high- z DOGs are diverse populations, ranging from merging galaxies to edge-on disk galaxies. We do not find clear evidence of evolution between subclasses (e.g., from SF-dominated DOGs to AGN-dominated DOGs). There are also some non-DOGs with a large AGN contribution (see Figure 7), suggesting that the amount of dust obscuration is not closely related to the presence of AGN. These results imply that DOGs are not in a unique phase of galaxy evolutionary sequence. Instead they seem to be the high-end tail of the dust obscuration distribution originating from various physical mechanisms.

7. CONCLUSIONS

By combining *GALEX* UV and *AKARI* / *WISE* MIR all-sky survey data, we identify 47 local analogs of DOGs with $S_{12\mu m} / S_{0.22\mu m} \geq 892$ and $S_{12\mu m} > 20$ mJy at $0.05 < z < 0.08$ in the SDSS DR7. We compare their physical properties with other 12 μm selected galaxies that do not satisfy DOG criteria to study how special the DOGs are among MIR selected galaxies. We also compare the physical properties of local DOGs with high- z DOGs. Our primary results are:

1. We fit the IR photometric data for local DOGs and the control sample with AGN/starburst SED templates to estimate their IR luminosities and the AGN contribution to their IR luminosities. Their total IR luminosities are in the range $3.4 \times 10^{10} (L_{\odot}) \lesssim L_{\text{IR}} \lesssim 7.0 \times 10^{11} (L_{\odot})$ with a me-

dian L_{IR} of $2.1 \times 10^{11} (L_{\odot})$. Among 47 DOGs, 20 (43%) have a relatively large AGN contribution (i.e., $f_{\text{AGN}} \geq 20\%$), and 27 (57%) DOGs with a small AGN contribution (i.e., $f_{\text{AGN}} < 20\%$).

2. Comparison of several flux density ratios between DOGs and the control sample indicates that the extreme flux density ratios between MIR and UV bands for DOGs result mainly from abnormal faintness in the UV rather than from extreme brightness in the MIR.
3. The i -band axis ratio distributions of DOGs and the control sample show that the fraction of galaxies with small axis ratios (i.e., < 0.6) among DOGs ($36 \pm 7\%$) is larger than that among the control sample ($17 \pm 3\%$). There is no obvious sign of interaction in the majority of DOGs. These results suggest, and optical images show, that some DOGs have large dust obscuration simply because of their high inclination.
4. The sSFRs of DOGs are similar to those of the control sample. However, these sSFRs are slightly larger than for typical IR bright galaxies at similar redshift by a factor of $\lesssim 2$. The DOGs with a large AGN contribution (e.g., $f_{\text{AGN}} \geq 20\%$) appear to have smaller sSFRs than those with a small AGN contribution (i.e., $f_{\text{AGN}} < 20\%$).
5. The large- and small-scale environments of DOGs are similar to those of the control sample and of other IR bright galaxies at similar redshift.

From the comparison between local and high- z DOGs, we find:

1. Many physical properties of local DOGs are similar to those of high- z DOGs, even though the IR luminosities of local DOGs are an order of magnitude lower than for the high- z counterparts. These properties include the presence of two classes (AGN- and SF-dominated) of DOGs, different properties between the two classes, abnormal faintness in the UV rather than extreme brightness in the MIR, and diverse optical morphology.
2. There are some differences between local and high- z DOGs. These differences include larger $L_{\text{H}\alpha} / L_{\text{IR, total}}$ for local DOGs than for high- z DOGs, few local DOGs with dust temperatures as low as high- z DOGs, and similar size distributions between AGN- and SF-dominated DOGs at low redshift in contrast with different distributions at high redshift. However, these differences may result from different IR luminosities and/or different selection effects.

Our results suggest that local DOGs indeed share a common underlying physical origin with high- z DOGs. Both local and high- z DOGs are diverse in nature. They seem to be in the high-end tail of the dust obscuration distribution. Their dusty nature results from a range of physical mechanisms rather than from a unique phase in the galaxy evolutionary sequence.

Some differences between local and high- z DOGs including the amount of dust obscuration and the dust temperature may result mainly from different IR luminosities and/or complex selection effects. To resolve this issue, it is necessary to have galaxy samples with similar IR luminosities by exploring larger local volumes with appropriate bands to access the rare luminous low- z DOGs. Deeper data sets could identify less luminous high- z DOGs to overlap the low- z sample. FIR and submillimeter data for larger number of DOGs in both low and high redshifts would mitigate the selection effects and would provide direct measures of dust mass and temperature.

We thank the anonymous referee for many insightful comments that improved the manuscript. HSH acknowledges the Smithsonian Institution for the support of his post-doctoral fellowship. The Smithsonian Institution also supports the research of MJG. This publication makes use of data products from the Wide-field Infrared Survey Explorer, which is a joint project of the University of California, Los Angeles, and the Jet Propulsion Laboratory/California Institute of Technology, funded by the National Aeronautics and Space Administration. This research is based on observations with AKARI, a JAXA project with the participation of ESA. Funding for the SDSS and SDSS-II has been provided by the Alfred P. Sloan Foundation, the Participating Institutions, the National Science Foundation, the U.S. Department of Energy, the National Aeronautics and Space Administration, the Japanese Monbukagakusho, the Max Planck Society, and the Higher Education Funding Council for England. The SDSS Web Site is <http://www.sdss.org/>. The SDSS is managed by the Astrophysical Research Consortium for the Participating Institutions. The Participating Institutions are the American Museum of Natural History, Astrophysical Institute Potsdam, University of Basel, Cambridge University, Case Western Reserve University, University of Chicago, Drexel University, Fermilab, the Institute for Advanced Study, the Japan Participation Group, Johns Hopkins University, the Joint Institute for Nuclear Astrophysics, the Kavli Institute for Particle Astrophysics and Cosmology, the Korean Scientist Group, the Chinese Academy of Sciences (LAMOST), Los Alamos National Laboratory, the Max-Planck-Institute for Astronomy (MPIA), the Max-Planck-Institute for Astrophysics (MPA), New Mexico State University, Ohio State University, University of Pittsburgh, University of Portsmouth, Princeton University, the United States Naval Observatory, and the University of Washington. This research has made use of the NASA/IPAC Extragalactic Database (NED) which is operated by the Jet Propulsion Laboratory, California Institute of Technology, under contract with the National Aeronautics and Space Administration.

REFERENCES

- Ahn, C. P., Alexandroff, R., Allende Prieto, C., et al. 2012, *ApJS*, 203, 21
- Amblard, A., Cooray, A., Serra, P., et al. 2010, *A&A*, 518, L9
- Baldwin, J. A., Phillips, M. M., & Terlevich, R. 1981, *PASP*, 93, 5
- Barton, E. J., Geller, M. J., & Kenyon, S. J. 2000, *ApJ*, 530, 660
- Behroozi, P. S., Wechsler, R. H., & Conroy, C. 2012, *ApJ*, submitted (arXiv:1207.6105)
- Berta, S., Fritz, J., Franceschini, A., Bressan, A., & Pernechele, C. 2003, *A&A*, 403, 119
- Blanton, M. R., & Moustakas, J. 2009, *ARA&A*, 47, 159
- Blanton, M. R., & Roweis, S. 2007, *AJ*, 133, 734
- Brand, K., Dey, A., Desai, V., et al. 2007, *ApJ*, 663, 204
- Brodwin, M., Dey, A., Brown, M. J. I., et al. 2008, *ApJ*, 687, L65
- Bruzual, G., & Charlot, S. 2003, *MNRAS*, 344, 1000
- Bussmann, R. S., Dey, A., Lotz, J., et al. 2009a, *ApJ*, 693, 750
- Bussmann, R. S., Dey, A., Borys, C., et al. 2009b, *ApJ*, 705, 184
- Bussmann, R. S., Dey, A., Lotz, J., et al. 2011, *ApJ*, 733, 21
- Bussmann, R. S., Dey, A., Armus, L., et al. 2012, *ApJ*, 744, 150
- Calzetti, D., Armus, L., Bohlin, R. C., et al. 2000, *ApJ*, 533, 682
- Chapin, E. L., Chapman, S. C., Coppin, K. E., et al. 2011, *MNRAS*, 411, 505
- Chapman, S. C., Blain, A. W., Smail, I., & Ivison, R. J. 2005, *ApJ*, 622, 772
- Chapman, S. C., Helou, G., Lewis, G. F., & Dale, D. A. 2003, *ApJ*, 588, 186
- Choi, Y., Han, D., & Kim, S. S. 2010, *J. Korean Astron. Soc.*, 43, 191
- Choi, Y., Park, C., & Vogeley, M. S. 2007, *ApJ*, 658, 884
- Cox, T. J., Jonsson, P., Somerville, R. S., Primack, J. R., & Dekel, A. 2008, *MNRAS*, 384, 386
- Daddi, E., Elbaz, D., Walter, F., et al. 2010a, *ApJ*, 714, L118
- Daddi, E., Bournaud, F., Walter, F., et al. 2010b, *ApJ*, 713, 686
- Desai, V., Soifer, B. T., Dey, A., et al. 2009, *ApJ*, 700, 1190
- Dey, A., Soifer, B. T., Desai, V., et al. 2008, *ApJ*, 677, 943
- Dickinson, M., Giavalisco, M., & GOODS Team. 2003, in *The Mass of Galaxies at Low and High Redshift*, ed. R. Bender & A. Renzini, 324+
- Donley, J. L., Rieke, G. H., Alexander, D. M., Egami, E., & Pérez-González, P. G. 2010, *ApJ*, 719, 1393
- Donoso, E., Yan, L., Tsai, C., et al. 2012, *ApJ*, 748, 80
- Elbaz, D., Daddi, E., Le Borgne, D., et al. 2007, *A&A*, 468, 33
- Elbaz, D., Hwang, H. S., Magnelli, B., et al. 2010, *A&A*, 518, L29
- Elbaz, D., Dickinson, M., Hwang, H. S., et al. 2011, *A&A*, 533, 119
- Fiore, F., Grazian, A., Santini, P., et al. 2008, *ApJ*, 672, 94
- Grogin, N. A., Kocevski, D. D., Faber, S. M., et al. 2011, *ApJS*, 197, 35
- Houck, J. R., Soifer, B. T., Weedman, D., et al. 2005, *ApJ*, 622, L105
- Hwang, H. S., Elbaz, D., Lee, J. C., et al. 2010a, *A&A*, 522, 33
- Hwang, H. S., Geller, M. J., Diaferio, A., & Rines, K. J. 2012a, *ApJ*, 752, 64
- Hwang, H. S., Geller, M. J., Kurtz, M. J., Dell'Antonio, I. P., & Fabricant, D. G. 2012b, *ApJ*, 758, 25
- Hwang, H. S., Park, C., Elbaz, D., & Choi, Y.-Y. 2012c, *A&A*, 538, 15
- Hwang, H. S., Elbaz, D., Magdis, G., et al. 2010b, *MNRAS*, 409, 75
- Hwang, H. S., Elbaz, D., Dickinson, M., et al. 2011, *A&A*, 535, 60
- Ishihara, D., Onaka, T., Kataza, H., et al. 2010, *A&A*, 514, 1
- Jarrett, T. H., Chester, T., Cutri, R., et al. 2000, *AJ*, 119, 2498
- Jarrett, T. H., Cohen, M., Masci, F., et al. 2011, *ApJ*, 735, 112
- Kartaltepe, J. S., Dickinson, M., Alexander, D. M., et al. 2012, *ApJ*, 757, 23
- Kauffmann, G., Heckman, T. M., White, S. D. M., et al. 2003a, *MNRAS*, 341, 33
- Kauffmann, G., Heckman, T. M., Tremonti, C., et al. 2003b, *MNRAS*, 346, 1055
- Kawada, M., Baba, H., Barthel, P. D., et al. 2007, *PASJ*, 59, 389
- Kennicutt, Jr., R. C. 1998, *ARA&A*, 36, 189
- Kewley, L. J., Dopita, M. A., Sutherland, R. S., Heisler, C. A., & Trevena, J. 2001, *ApJ*, 556, 121
- Kewley, L. J., Groves, B., Kauffmann, G., & Heckman, T. 2006, *MNRAS*, 372, 961
- Kewley, L. J., Jansen, R. A., & Geller, M. J. 2005, *PASP*, 117, 227
- Kirkpatrick, A., Pope, A., Alexander, D. M., et al. 2012, *ApJ*, 759, 139
- Kirkpatrick, A., Pope, A., Charmandaris, V., et al. 2013, *ApJ*, 763, 123
- Knapp, G. R., Guhathakurta, P., Kim, D.-W., & Jura, M. A. 1989, *ApJS*, 70, 329
- Ko, J., Hwang, H. S., Lee, J. C., & Sohn, Y.-J. 2013, *ApJ*, 767, 90

- Kovács, A., Chapman, S. C., Dowell, C. D., et al. 2006, *ApJ*, 650, 592
- Kroupa, P. 2001, *MNRAS*, 322, 231
- Lee, J. C., Hwang, H. S., Lee, M. G., Kim, M., & Lee, J. H. 2012, *ApJ*, 756, 95
- Lee, J. H., Hwang, H. S., Lee, M. G., Lee, J. C., & Matsuhara, H. 2010, *ApJ*, 719, 1946
- Lonsdale, C. J., Polletta, M. d. C., Omont, A., et al. 2009, *ApJ*, 692, 422
- Magdis, G. E., Elbaz, D., Hwang, H. S., et al. 2010, *MNRAS*, 409, 22
- Magdis, G. E., Daddi, E., Béthermin, M., et al. 2012, *ApJ*, 760, 6
- Magnelli, B., Lutz, D., Santini, P., et al. 2012, *A&A*, 539, A155
- Martin, D. C., Fanson, J., Schiminovich, D., et al. 2005, *ApJ*, 619, L1
- Mateos, S., Alonso-Herrero, A., Carrera, F. J., et al. 2012, *MNRAS*, 426, 3271
- Melbourne, J., Bussman, R. S., Brand, K., et al. 2009, *AJ*, 137, 4854
- Melbourne, J., Peng, C. Y., Soifer, B. T., et al. 2011, *AJ*, 141, 141
- Melbourne, J., Soifer, B. T., Desai, V., et al. 2012, *AJ*, 143, 125
- Moshir, M., Kopman, G., & Conrow, T. A. O. 1992, *IRAS Faint Source Survey*, Explanatory supplement version 2
- Mullaney, J. R., Alexander, D. M., Goulding, A. D., & Hickox, R. C. 2011, *MNRAS*, 414, 1082
- Murakami, H., Baba, H., Barthel, P., et al. 2007, *PASJ*, 59, 369
- Narayanan, D., Dey, A., Hayward, C. C., et al. 2010, *MNRAS*, 407, 1701
- Neugebauer, G., Habing, H. J., van Duinen, R., et al. 1984, *ApJ*, 278, L1
- Obrić, M., Ivezić, Ž., Best, P. N., et al. 2006, *MNRAS*, 370, 1677
- Osterbrock, D. E., & Ferland, G. J. 2006, *Astrophysics of Gaseous Nebulae and Active Galactic Nuclei*, ed. Osterbrock, D. E. & Ferland, G. J.
- Park, C., & Choi, Y. 2009, *ApJ*, 691, 1828
- Park, C., Gott, J. R. I., & Choi, Y. 2008, *ApJ*, 674, 784
- Penner, K., Dickinson, M., Pope, A., et al. 2012, *ApJ*, 759, 28
- Polletta, M., Tajer, M., Maraschi, L., et al. 2007, *ApJ*, 663, 81
- Pope, A., Bussmann, R. S., Dey, A., et al. 2008, *ApJ*, 689, 127
- Reddy, N., Dickinson, M., Elbaz, D., et al. 2012, *ApJ*, 744, 154
- Reddy, N. A., Steidel, C. C., Pettini, M., et al. 2008, *ApJS*, 175, 48
- Ree, C. H., Lee, Y.-W., Yi, S. K., et al. 2007, *ApJS*, 173, 607
- Sajina, A., Yan, L., Fadda, D., Dasyra, K., & Huynh, M. 2012, *ApJ*, 757, 13
- Salpeter, E. E. 1955, *ApJ*, 121, 161
- Sargent, M. T., Daddi, E., Béthermin, M., et al. 2013, *ApJ*, submitted (arXiv:1303.4392)
- Schawinski, K., Simmons, B. D., Urry, C. M., Treister, E., & Glikman, E. 2012, *MNRAS*, 425, L61
- Skrutskie, M. F., Cutri, R. M., Stiening, R., et al. 2006, *AJ*, 131, 1163
- Smith, M. W. L., Gomez, H. L., Eales, S. A., et al. 2012, *ApJ*, 748, 123
- Stern, D., Assef, R. J., Benford, D. J., et al. 2012, *ApJ*, 753, 30
- Swinbank, A. M., Smail, I., Chapman, S. C., et al. 2004, *ApJ*, 617, 64
- Symeonidis, M., Vaccari, M., Berta, S., et al. 2013, *MNRAS*, in press (arXiv:1302.4895)
- Tacconi, L. J., Genzel, R., Neri, R., et al. 2010, *Nature*, 463, 781
- Takata, T., Sekiguchi, K., Smail, I., et al. 2006, *ApJ*, 651, 713
- Tyler, K. D., Le Floc'h, E., Rieke, G. H., et al. 2009, *ApJ*, 691, 1846
- Veilleux, S., & Osterbrock, D. E. 1987, *ApJS*, 63, 295
- Veilleux, S., Rupke, D. S. N., Kim, D., et al. 2009, *ApJS*, 182, 628
- Woods, D. F., & Geller, M. J. 2007, *AJ*, 134, 527
- Wright, E. L., Eisenhardt, P. R. M., Mainzer, A. K., et al. 2010, *AJ*, 140, 1868
- Wu, J., Tsai, C.-W., Sayers, J., et al. 2012, *ApJ*, 756, 96
- Wyder, T. K., Martin, D. C., Schiminovich, D., et al. 2007, *ApJS*, 173, 293
- Yan, L., Helou, G., Fadda, D., et al. 2004, *ApJS*, 154, 60
- Yang, M., Greve, T. R., Dowell, C. D., & Borys, C. 2007, *ApJ*, 660, 1198
- York, D. G., Adelman, J., Anderson, Jr., J. E., et al. 2000, *AJ*, 120, 1579
- Younger, J. D., Omont, A., Fiolet, N., et al. 2009, *MNRAS*, 394, 1685